Diabatic processes and the evolution of two contrasting summer extratropical cyclones

Oscar Martínez-Alvarado *

National Centre for Atmospheric Science–Atmospheric Physics, United Kingdom and

Department of Meteorology, University of Reading, Reading, United Kingdom

Suzanne L. Gray and John Methven

Department of Meteorology, University of Reading, Reading, United Kingdom

ABSTRACT

Two extratropical cyclones were observed in July and August 2012 with a research aircraft during the fourth field campaign of the DIAMET (DIAbatic influences on Mesoscale structures in ExTratropical storms) project. Even though both cyclones were slow moving and produced intense precipitation, they represented very different synoptic conditions. The first cyclone, observed during the Intense Observation Period (IOP) 13, deepened only down to 995 hPa; the second cyclone, observed during the IOP 14, deepened down to 978 hPa and formed a potential vorticity (PV) tower. The objectives of this contribution are to quantify the effects of diabatic processes on cyclone cross-isentropic mass transport and circulation, as well as the contribution of relevant parametrization schemes to these effects. The cyclones were analyzed through numerical simulations incorporating tracers for the effects of diabatic processes on potential temperature and PV, which were separated into materially-conserved and diabatically-generated parts. The simulations were compared with radar rainfall observations and dropsonde measurements obtained during the IOPs. It was found that diabatic effects were primarily produced through the parametrizations schemes of boundary layer and turbulent mixing, cloud microphysics and convection in both cases, but all these parametrizations, and convection in particular, were more active in IOP14 than in IOP13. It is shown that diabatic effects on the circulation can only occur if there is an imbalance between the isentropic fluxes of the materially-conserved and diabatically-generated PV. This imbalance occurs much more in IOP14 than in IOP13, leading to the former being a more dynamically active system.

1. Introduction

The passage of extratropical cyclones over Northern Europe in summer is associated with enhanced precipitation, as moist air is forced to ascend along the cyclones' warm and cold conveyor belts. Using data from the Global Precipitation Climatology Product daily precipitation dataset (Huffman et al. 2001; Adler et al. 2003) and the ECMWF ERA-Interim reanalysis product (Simmons et al. 2007; Dee et al. 2011), Hawcroft et al. (2012) determined that more than 65% of total precipitation during June–July–August is associated with extratropical cyclones over the United Kingdom, Northern Europe and Scandinavia. Heavy precipitation can have an important societal impact as it can lead to extreme weather events such as flash flooding. Water vapor condensation in the rising air also releases latent heat, which typically intensifies the ascending motion and the cyclone near the surface. Studying a cyclone that reached its maximum intensity on 24 February 1987, Stoelinga (1996) showed that its intensity was 70% stronger as a result of coupling between baroclinic wave growth and latent heat release. However, the importance of latent heat release, and diabatic processes in general, for the development of summer extratropical cyclones has received much less attention. Summer extratropical cyclones are generally less frequent and weaker than their winter counterparts. They also exhibit a narrower range in terms of intensity. In an analysis of the ERA-Interim dataset between 1989 and 2009, Čampa and Wernli (2012) showed that the central mean sea level pressure of winter cyclones in the Northern Hemisphere can be found in the range between 930 hPa and 1030 hPa; Northern Hemisphere summer cyclones can be found in the same range, but are largely concentrated around 990 hPa and 1010 hPa.

This article has two objectives. The first objective is to quantify the total heating produced during the occurrence of two summer extratropical cyclones and assess the effects of this heating in terms of changes to the circulation around the cyclones. The second objective is to determine the contribution that each relevant parametrization scheme made to the total heating and its effects in these two cyclones. These objectives are pursued through simulations with a numerical model that requires the parametrization of con-

vection. The model includes tracers of diabatic effects on potential temperature (θ) (e.g. Martínez-Alvarado and Plant 2014) and potential vorticity (PV) (e.g. Stoelinga 1996; Gray 2006).

The two cyclones in this study occurred during the last field campaign of the DIAMET (DIAbatic influences on Mesoscale structures in ExTratropical storms) project (Vaughan et al. 2015), which took place in the summer of 2012. Dearden et al. (2015) use the same two cases to examine the effect of ice phase microphysical processes on the dynamics of summer extratropical cyclones. Both cyclones were slow-moving systems with developed bent-back fronts. Moreover, both cyclones exhibited prolonged periods of heavy frontal precipitation (Fig. 1(a,d)). Despite these similarities, the two cyclones represent two very different intensity scenarios for summer. The first cyclone reached a central pressure minimum of 995 hPa on 19 July 2012. Its central pressure places it in the most frequent cyclone category for summer cyclones over western Europe (Čampa and Wernli 2012): five out of an average of seven annual summer cyclones that reach maximum intensity over western Europe have an intensity between 990 hPa and 1010 hPa (Table 1). In contrast, the second cyclone reached a central pressure minimum of 978 hPa on 15 August 2012. Only 0.8 summer cyclones per year on average have an intensity between 970 hPa and 990 hPa (Table 1). Given its intensity, this cyclone would be more typical of winter than summer (Table 1).

The rest of the article is organized as follows. The available aircraft observations, numerical model and diabatic tracers are described in Section 2; Section 3 is devoted to the comparison of the simulations with the available observations. The results are presented and discussed in Sections 4 and 5, which deal with the July and August cases, respectively, and in Section 6, which makes a comparison in terms of diabatic processes between the two cyclones. Finally, a summary and conclusions are given in Section 7.

2. Data and methods

a. Available aircraft observations

The two cyclones occurred during the fourth field campaign of the DIAMET project (Vaughan et al. 2015). The cyclone on 18 July 2012 was the subject of the DIAMET Intensive Observation Period (IOP) 13 while the cyclone on 15 August 2012 was the subject of the DIAMET IOP14. Both cyclones were observed with the instruments on board the Facility for Airborne Atmospheric Measurements (FAAM) BAe146 research aircraft. A summary of the instruments, their sampling frequency and uncertainty on output parameters is given in Vaughan et al. (2015). Dropsondes (Vaisala AVAPS RD94) were launched from approximately 400 hPa. The dropsondes measured temperature, pressure and specific humidity as a function of latitude, longitude and time (at a sampling frequency of 2 Hz). Horizontal wind profiles were obtained by GPS tracking of the dropsondes (logged at 4 Hz). Two sondes could be logged on the aircraft at any one time, and the average time for sonde descent was 10 minutes, limiting the average sonde spacing to a minimum of 4 minutes along the flight track or 24 km at the aircraft science speed of 100 m s^{-1}. The vertical resolution is about 10 m. Table 2 lists the sonde release times along the dropsonde curtains used in Section 3 to compare these observations with the simulations described below.

b. Hindcast simulations

The simulations have been performed using the MetUM version 7.3 which is based on the so-called "New Dynamics" dynamical core (Davies et al. 2005). It is a finite-difference model that solves the non-hydrostatic deep-atmosphere dynamical equations with a semi-implicit, semi-Lagrangian integration scheme (Davies et al. 2005). It uses Arakawa C staggering in the horizontal (Arakawa and Lamb 1977) and is terrain-following with a hybrid-height Charney and Phillips (1953) vertical coordinate. Parametrization of physical processes includes longwave and shortwave radiation (Edwards and Slingo 1996), boundary layer (BL) and turbulent mixing (Lock et al. 2000), cloud microphysics and large-scale precipitation (Wilson and Ballard 1999) and convection (Gregory and Rowntree 1990).

The simulations have been performed on a limited-area domain corresponding to the Met Office's recently operational North-Atlantic–European domain with 600×300 grid points. The horizontal grid spacing is $0.11°$ (~ 12 km) in both longitude and latitude on a rotated grid centered around 52.5°N, 2.5°W. The North-Atlantic–European domain extends approximately from 30°N to 70°N in latitude and from 60°W to 40°E in longitude. The vertical coordinate is discretized in 70 vertical levels with lid around 80 km. The initial conditions were given by native Met Office operational analyses to minimize the effects of 'initial shocks' (Klocke and Rodwell 2013). The analyses used were those valid at 1200 UTC 17 July 2012, for IOP13, and at 1800 UTC 14 August 2012, for IOP14. The lateral boundary conditions consisted of the Met Office operational 3-hourly lateral boundary conditions valid from 0900 UTC 17 July 2012 for 72 hours, for IOP13, and from 1500 UTC 14 August 2012 for 72 hours, for IOP14. The results presented in this work correspond to simulations of 21 hours for both cyclones.

c. Diabatic tracers

The MetUM has been enhanced by the inclusion of diabatic tracers of θ and PV. Diabatic tracers track θ and PV changes due to diabatic processes. Potential temperature tracers enable identification of the processes (includ-

Table 1: Number of cyclones over western Europe in summer (June–July–August) and winter (December–January–February) in the ERA-Interim dataset for the period between 1989 and 2009. The definition of western Europe and the frequency columns were taken from Čampa and Wernli (2012).

	Summer		Winter	
	Number of cyclones	Occurrence per year	Number of cyclones	Occurrence per year
930–970 hPa	1	0.05	33	1.65
970–990 hPa	16	0.80	64	3.20
990–1010 hPa	99	4.95	75	3.75
1010–1030 hPa	15	0.75	10	0.50
Total	131	6.55	182	9.10

Table 2: Dropsonde release times

IOP13								
Dropsonde No.	1	2	3	4	5	6	7	8
Release time (UTC)	0830	0834	0838	0842	0846	0854	0858	0902
IOP14								
Dropsonde No.	1	2	3	4	5	6	7	8
Release time (UTC)	1534	1538	1543	1547	1551	1555	1559	1603

ing turbulent mixing and resolved advection) that bring air parcels to their current isentropic level through cross-isentropic motion. PV tracers enable identification of modifications to the circulation and stability and the diabatic processes responsible for such modifications. The θ tracers have been previously described in Martínez-Alvarado and Plant (2014) and Martínez-Alvarado et al. (2014b), while the PV tracers have been previously described in Stoelinga (1996), Gray (2006), Chagnon and Gray (2009) and Chagnon et al. (2013). Both kinds of tracers have been used together in the analysis of forecast errors in upper-level Rossby waves (Martínez-Alvarado et al. 2015).

The idea behind both kinds of tracers consists of the separation of the variable of interest φ (representing either θ or PV) into the sum of a materially-conserved component, φ_0, a diabatically-generated component, φ_d, and a residual, r_φ, i.e.

$$\varphi(\boldsymbol{x},t) = \varphi_0(\boldsymbol{x},t) + \varphi_\mathrm{d}(\boldsymbol{x},t) + r_\varphi(\boldsymbol{x},t), \tag{1}$$

where $\boldsymbol{x}$ represents spatial location and t is time. The materially-conserved and the diabatically-generated parts are governed by the following equations

$$\frac{D\varphi_0}{Dt} = 0 \tag{2}$$

$$\frac{D\varphi_\mathrm{d}}{Dt} = S_\varphi, \tag{3}$$

where S_φ represents a source due to diabatic processes,

$$\frac{D}{Dt} = \frac{\partial}{\partial t} + \boldsymbol{v}\cdot\nabla,$$

and $\boldsymbol{v} = (u, v, w)$ is the three-dimensional velocity field. In other words, φ_0 is unaffected by diabatic processes, and therefore conserved following an air parcel, while φ_d is affected by diabatic processes. Since φ_0 is only affected by advection, this tracer has also been called an *advection-only* tracer in other works (Chagnon et al. 2013; Chagnon and Gray 2015). The sum of (2) and (3) yields the full evolution equation for φ. At initialisation time, t_0, $\varphi_0(\boldsymbol{x},t_0) = \varphi(\boldsymbol{x},t_0)$ and $\varphi_\mathrm{d}(\boldsymbol{x},t_0) = 0$. The boundary conditions for φ_0 are the boundary conditions for φ while those for φ_d are set to zero.

Diabatic tracers can be further extended to the analysis of individual diabatic processes by separating φ_d into a series of tracers φ_p

$$\varphi_\mathrm{d} = \sum_{p\in\{\mathrm{proc}\}} \varphi_p, \tag{4}$$

where {proc} is the set of parametrized diabatic processes in the model. In this work we consider contributions from four parametrized processes, namely (i) BL and turbulent mixing processes, (ii) convection, (iii) cloud microphysics including condensation and (iv) radiation. The contribution from gravity wave drag to the modification of PV has also been computed, but is much smaller in comparison with processes (i)–(iv) and therefore it is not shown. Each tracer is selectively affected by the p-th parametrized process and governed by the equation

$$\frac{D\varphi_p}{Dt} = S_{\varphi,p}, \tag{5}$$

where $S_{\varphi,p}$ represents the source due to the p-th parametrized

process so that

$$S_\varphi = \sum_{p\in\{\text{proc}\}} S_{\varphi,p}. \tag{6}$$

Equations (2), (3) and (5) are solved using the same numerical methods implemented in the MetUM to solve the evolution equations of the model's prognostic variables (cf. Davies et al. 2005). However, details within such numerical methods, such as the staggered distribution of the variables on the Arakawa C-grid (Whitehead et al. 2014) and the treatment of vertical interpolation in the advection of θ (Davies et al. 2005), are only strictly valid for the prognostic variables themselves. Therefore, there is an unavoidable mismatch between the computation of advection for the prognostic variables and for diabatic tracers, which gives rise to the residual term in (1). The residual grows over time in both cases, but at a slower rate for the θ tracers than for PV tracers. However, restricting the length of the simulations to 24 hours also restricts the residual growth to a maximum of ± 2 K for θ and ± 3 PVU for PV in localized areas within the domain.

d. Integral interpretation of θ tracers: Cross-isentropic mass transport

Given that the θ_0 tracer is materially-conserved and represents the θ field at the start of the simulation, it can be used as a Lagrangian label for the vertical position (in isentropic coordinates) of air masses at the start of the simulation. An integral interpretation of the θ tracers can be achieved by analyzing the evolution of the θ_0 tracer within volumes around the cyclones' centers. Thus, for each considered time, the grid points within a 1000-km radius 'cylinder' centered at the cyclone's center were classified according to their θ_0-value into seven 10-K width bins with centers at $\theta_0 = 275 + 10k$ [K] for $k = 0, 1, \ldots, 6$. This operation produces a population of grid points for each θ_0-bin, which can then be analyzed separately. The θ_0 distributions were computed hourly from the first hour of each simulation until the end of each simulation (i.e. 21 hours). This methodology is applied in Section 6a to determine the range of the θ changes for each θ_0-bin, and the contributions from individual diabatic processes to these changes, as a function of time in each cyclone.

e. Integral interpretation of PV tracers: Circulation

PV is defined in geographic coordinates as (e.g. Haynes and McIntyre 1987)

$$Q = \frac{1}{\rho}\nabla\times\boldsymbol{u}\cdot\nabla\theta, \tag{7}$$

where ρ is density and $\boldsymbol{u}$ is the three-dimensional absolute velocity. The absolute circulation on an isentropic surface is given by

$$C = \oint_C \boldsymbol{u}\cdot d\boldsymbol{l} = \int_R \nabla\times\boldsymbol{u}\cdot\boldsymbol{k}_\theta\, dS, \tag{8}$$

where C is a closed contour on the isentropic surface enclosing region R, $d\boldsymbol{l}$ is a line element on contour C, dS is a surface element on region R and $\boldsymbol{k}_\theta$ is a unit vector normal to the isentropic surface. $\boldsymbol{k}_\theta$ can be written in terms of $\nabla\theta$ as

$$\boldsymbol{k}_\theta = \frac{\nabla\theta}{|\nabla\theta|}, \tag{9}$$

while dS is given by

$$dS = \left(\frac{\partial\theta}{\partial z}\right)^{-1} |\nabla\theta|\, dx\, dy, \tag{10}$$

z is geopotential height and $\nabla = (\partial_x, \partial_y, \partial_z)$ is the gradient in geographic coordinates. This expression is valid as long as θ is a monotonically increasing function of height, i.e. as long as θ can be used as a vertical coordinate. Substituting (9) and (10) into (8) yields

$$C = \int_R \left(\frac{\partial\theta}{\partial z}\right)^{-1} \nabla\times\boldsymbol{u}\cdot\nabla\theta\, dx\, dy. \tag{11}$$

Using (7) and defining the isentropic density as

$$\sigma = \rho\left(\frac{\partial\theta}{\partial z}\right)^{-1}, \tag{12}$$

we can write

$$C = \int_R \sigma\, Q\, dxdy. \tag{13}$$

Using (1) PV can be written as

$$Q = Q_0 + Q_\mathrm{d} + r_Q, \tag{14}$$

where Q_0, Q_d and r_Q are the materially-conserved, the diabatically-generated and the residual parts of PV, respectively. Multiplying (14) by σ and integrating over the isentropic region R we obtain

$$C = C_0 + C_\mathrm{d} + C_\mathrm{r}, \tag{15}$$

where

$$C_0 = \int_R \sigma\, Q_0 dx\, dy \quad \text{and} \quad C_\mathrm{d} = \int_R \sigma\, Q_\mathrm{d} dx\, dy, \tag{16}$$

i.e. Q_0 and Q_d induce contributions to the circulation on isentropic surfaces that can be directly associated with the materially-conserved and the diabatically-generated parts of PV. The contribution associated with the residual is assumed small and can be computed as $C_\mathrm{r} = C - (C_0 + C_\mathrm{d})$. Dividing (15) by $\int_R dx\, dy$ we obtain

$$\zeta_\theta = \zeta_{\theta,0} + \zeta_{\theta,\mathrm{d}} + \zeta_{\theta,\mathrm{r}}, \tag{17}$$

where ζ_θ is area-averaged isentropic vorticity, $\zeta_{\theta,0}$ and $\zeta_{\theta,\mathrm{d}}$ are the contributions associated with the materially-conserved and diabatically-generated parts of PV, respectively, and $\zeta_{\theta,\mathrm{r}}$ is the contribution associated with r_Q. These results are valid for any isentropic surface. However, the computations can be carried out for a set of isentropic levels at different time steps to construct time series of vertical profiles for ζ_θ, $\zeta_{\theta,0}$ and $\zeta_{\theta,\mathrm{d}}$, as is done in Section 6a.

3. Comparison between simulations and observations

The two extratropical cyclones in this study exhibited similarities. Both cyclones moved slowly: the IOP13 cyclone travelled around 600 km during 18 July 2012; the IOP14 cyclone travelled around 700 km during 15 August 2012. Furthermore, both cyclones produced precipitation for prolonged periods. Precipitation associated with the IOP13 cyclone started around 1800 UTC 17 July 2012 over Northern Ireland and ended at around 0100 UTC 19 July 2012 across northern England. Figure 1a shows radar rainfall rates at 0900 UTC 18 July 2012. It shows heavy precipitation on a band over Scotland, corresponding to the detached warm front, and scattered precipitation over the south-east of England, corresponding to weak precipitation at the cold front. Precipitation associated with the IOP14 cyclone started before 0000 UTC 15 August 2012 and continued for the day, sweeping the United Kingdom and Ireland from south to north (Fig. 1d). These features were well represented by the simulations. Figure 1b shows the rainfall rate for IOP13 derived from the simulation corresponding to the time shown in Fig. 1a (i.e. T+21). Figure 1e shows the corresponding rainfall rate for IOP14 for the time shown in Fig. 1d (i.e. T+22). In both cases, the simulations compare well with radar observations in terms of location and intensity of precipitating features, bar differences in the resolutions of both datasets. However, one feature that the model fails to represent is the clear split into two precipitation bands over the east of England in IOP14 due to the gap between the system's cold and warm fronts (Fig. 1d).

Despite the similarities in speed and precipitation, both cyclones represent very different synoptic conditions. Figure 1c shows the synoptic chart for IOP13 at 0600 UTC 19 July 2012. The IOP13 cyclone was a shallow system with a triple point located at the low-pressure center. The cyclone deepened slightly after the time shown, reaching 995 hPa at 0600 UTC 19 July 2012. However, its structure remained largely the same from 0600 UTC 18 July 2012 until the end of its life cycle. In contrast, the cyclone in IOP14 was a relatively deep system for a summer cyclone. Figure 1f shows the IOP14 cyclone at 1200 UTC 15 August 2012 with its bent-back front (analyzed as an occluded front) wrapped up around the system's low-pressure center. These features were also well represented by the simulations as indicated by the 850-hPa isolines of equivalent potential temperature, θ_e, in Figs. 1(b,e).

Figures 2(a,c) show vertical cross sections of several quantities derived from the dropsondes during the first IOP13 leg (see Table 2). Figure 2a shows zonal velocity, u, θ and relative humidity w.r.t. ice, $\mathrm{RH_{ice}}$; Fig. 2c shows θ_e and water vapor flux defined as $\phi_q = \rho q v_H$, where q is specific humidity and v_H is the horizontal wind component across the section. Easterly winds of more than 10 m s^{-1} are confined below 900 hPa. These winds are located around 57.5°N within a region of strong horizontal θ_e gradient, which corresponds to the system's warm front (Fig. 2c). Westerly winds of similar magnitude, located south of the warm front, extend to pressures as low as 650 hPa. A column with $\mathrm{RH_{ice}} > 90\%$ extends from the surface to pressures around 450 hPa. This combination of u and $\mathrm{RH_{ice}}$ leads to the maximum westward ϕ_q being confined below 900 hPa within the warm front region, between 57°N and 58°N. The westward ϕ_q in Fig. 2c produces a total westward water vapor flow across the vertical dropsonde curtain below 7 km ($\sim$ 400 hPa) of $\Phi_{q,\mathrm{IOP13}} = 1.99 \times 10^7$ kg s^{-1}.

Figures 2(b,d) show vertical sections through segment A–B (Fig. 1b) for the same quantities as in Figs. 2(a,c), but derived from the simulation at 0900 UTC 18 July 2012 (T+21). Segment A–B approximately corresponds to the aircraft's track during the first IOP13 dropsonde leg. Zonal velocity has similar magnitude in model and observations (Fig. 2b). However, the region of maximum easterlies extends further up in the model than in observations, reaching 850 hPa. The column with $\mathrm{RH_{ice}} > 90\%$ also extends higher in the model than in observations, indicating that the model's atmosphere is too moist. This wet bias is a deficiency that has been previously identified in other studies using the MetUM version 7.3 (e.g Martínez-Alvarado et al. 2014a). A systematic wet bias in a model could be leading to an overestimation of warm conveyor belt (WCB) intensities and outflow levels as well as tropopause height (Schäfler and Harnisch 2015). However, it is not possible to quantify these effects with the available observations. The position of the warm front is similar in model and observations (Fig. 2d). However, the gradient of θ_e is stronger in the model, especially below 800 hPa. The vertical structure of ϕ_q is also similar in model and observations: The maximum westward ϕ_q is located within the region of maximum θ_e gradient and confined below 900 hPa (Fig. 2d). However, its magnitude is around 50% stronger in the model than in observations, as a result of stronger u and higher moisture availability in the model than in observations. Thus, $\Phi_{q,\mathrm{IOP13,sim}} = 4.40 \times 10^7$ kg s^{-1} according to the model, i.e. more than twice as much as in the observations.

Now we compare the dropsonde observations obtained during IOP14 with the simulation at 1600 UTC 15 July

2012 (T+22). Figure 3 shows the vertical structure of u, θ and $\mathrm{RH_{ice}}$ (Fig. 3a), and ϕ_q and θ_e (Fig. 3c). In this case, the flow moves westwards across the whole dropsonde curtain (Fig. 3a). The maximum zonal velocity ($|u| > 30$ m s^{-1}) is located at mid-tropospheric levels around 450 hPa. At lower levels, the maximum zonal velocity ($|u| > 20$ m s^{-1}) is located towards the section's northern edge behind the system's cold front, located around 55.5°N near the surface (Fig. 3c). This location corresponds to the low level jet and the system's WCB. A column with $\mathrm{RH_{ice}} > 90\%$ extends over the cold front to the upper part of the vertical section (Fig. 3a). Due to this combination of zonal velocity and moisture, ϕ_q exhibits maximum intensity ($|\phi_q| > 0.25$ kg m^{-2} s^{-1}) towards the section's northern edge (Fig. 3c). This flux produces a total westward water vapor flow across the vertical curtain below 7 km of $\Phi_{q,\mathrm{IOP14}} = 1.17\times10^8$ kg s^{-1}. This value is comparable to the typical meridional water vapor flow in a Northern Hemisphere atmospheric river $\Phi_{q,\mathrm{AR}} = 2.2 \times 10^8$ kg s^{-1} (Zhu and Newell 1998). Figure 3 also shows vertical sections for model-derived variables through segment C–D (Fig. 1e), which corresponds to the aircraft's track during the IOP14 dropsonde leg. In the model, the low-level jet core ($|u| > 25$ m s^{-1}) appears in the section around 55.5°N confined below 800 hPa (Fig. 3b). Like in IOP13, the column with $\mathrm{RH_{ice}} > 90\%$ spans a larger area within the section in the model than in the observations. However, in this case, this can be due to a mismatch between the position of the system's cold front, which in the model is located further south (around 54.5°N) than in the observations. The zonal velocity and vapor fields in the model produce a maximum vapor flux in IOP14 twice as strong as in IOP13.

4. Diabatic effects in IOP13

Figure 4 shows θ_0, which can be interpreted as a representation of cross-isentropic mass transport, and 2-PVU contours in IOP13 on the 319-K and 305-K isentropic levels to illustrate the synoptic situation at upper and lower levels, respectively. On the 319-K isentropic level (Fig. 4a) the 2-PVU contour represents the intersection of the surface with the tropopause. Thus, Ireland and part of Great Britain are located beneath stratospheric air while the south of England and the north of Scotland are located beneath tropospheric air. On this isentropic level, there is a band of strong cross-isentropic ascent spanning a sector from the north-west to the south-east of the cyclone center. This band of cross-isentropic ascent corresponds to the system's WCB outflow. The air mass constituting the WCB outflow was located within the BL, at levels with $\theta_0 < 290$ K, at the start of the simulation. However, most of the cross-isentropically ascending air originates within the lower and middle free troposphere (above the BL), from the layer $290 < \theta_0 < 320$ [K]. Outside the WCB outflow region, cross-isentropic subsidence is found not only in the stratospheric region that constitutes the descending air within the dry intrusion to the south and west of the cyclone center, but through most of the troposphere as well. The average cross-isentropic subsidence corresponds to an average cooling rate of 1.3 K day^{-1}, which is consistent with radiative cooling (Haynes et al. 2013). On the 305-K isentropic level (Fig. 4b) the 2-PVU contour represents low-level positive PV anomalies, which are usually of diabatic origin. One such an anomaly, shaped as an elongated east-west strip, is located immediately to the north of the cyclone's center. On this isentropic level, cross-isentropic ascent predominates to the north of the cyclone center. This region of cross-isentropic ascent is located over the system's warm front and is therefore part of the same cross-isentropically ascending WCB in Fig. 4a. Cross-isentropic subsidence surrounds the region of cross-isentropic ascent.

Figure 5 shows θ_0 and diabatically-generated PV on vertical sections along segment E–F in Fig. 4, which is a north–south cross section through the cyclone's center. The figure also shows 2-PVU contours and θ contours to allow comparison with Fig. 4. Figure 6 shows the partition of diabatic PV into contributions from parametrized processes in IOP13, as well as contours for PV = 2 PVU and θ to facilitate comparisons with Figs. 4–5. There are three regions in the cross sections that deserve comment, namely the system's WCB, low-level PV anomalies and the region close to the tropopause.

The system's WCB is unambiguously the cyclone's air stream that has experienced the most intense heating. Figure 5a displays a deep column of air in the interval $290 < \theta_0 < 300$ [K] extending from around 700 hPa up to near tropopause level around 300 hPa (320 K). The column is flanked to the south by the system's cold front, which by this time is already occluded, and to the north by the system's warm front. Comparisons of the intersections of this column with the 305-K and 319-K isentropic surfaces with those shown in Fig. 4 confirm that this is indeed part of the system's WCB.

The low-level PV anomaly, which in the 305-K isentropic surface appears as an elongated east–west feature, extends from the surface up to at least the 310-K isentropic level (500-hPa isobaric level) in this section. This low-level PV anomaly has been diabatically generated. Figure 5b shows that the PV within the anomaly has increased by more than 2 PVU due to diabatic activity. The lower part of the low-level PV anomaly (below 750 hPa) exhibits negligible θ change (not shown). Yet, it shows strong changes in PV due to BL and turbulent mixing processes (Fig. 6a). This part of the low-level PV anomaly is constituted by air that, moving quasi-isentropically, has travelled through the regions of PV production induced by BL heating. The upper part of the low-level PV anomaly (above 750 hPa) exhibits a small but positive θ change in the in-

terval $0 < \Delta\theta \leq 10$ [K] (not shown). The analysis of the contribution to θ changes due to diabatic processes shows that this part of the low-level PV anomaly is constituted by air that ascended cross-isentropically due to BL processes. The cross-isentropic ascent was weakened by cooling cloud microphysical processes. The PV was modified as the cross-isentropically ascending air travelled through regions of PV production induced first by BL and turbulent mixing processes (Fig. 6a) and second by cloud microphysical processes taking place inside the WCB cloud (Fig. 6c).

There are also shallow low-level regions of positive diabatically-generated PV below 800 hPa, particularly visible to the north of 58°N (Fig. 5b). These regions of positive diabatically-generated PV are generated by radiative cooling due to low-level clouds at the BL top. Although the air in this region is subject to BL and mixing processes, which tend to increase θ, this increase is overcome by radiative cooling which produces a net, albeit weak, cross-isentropic descent. The cross-isentropically descending air parcels are subject to negative and then positive PV production induced by the BL and turbulent mixing processes (Fig. 6a). At the same time they are subject to the opposite sequence, i.e. positive then negative PV production, induced by radiative cooling (Fig. 6d). The effects induced by radiation have greater magnitude than those induced by heating within the BL so that the net effect in the final diabatically-generated PV is a dipole structure with positive on top of negative diabatically-generated PV (see Fig. 5b).

The tropospheric air near the tropopause is characterized by a PV loss spanning a large section between 52°N and 59°N and between 310 K and 322 K (Fig. 5b). The region north of 56°N, between 315 K and 325 K, exhibits strong θ change in the interval $0 < \Delta\theta \leq 40$ [K] (Fig. 5a). This region is located within the WCB outflow. The PV modification is primarily due to BL and turbulent mixing processes (Fig. 6a) and occurs as cross-isentropically ascending air travelled through regions of negative PV production induced by heating within the BL. Cloud microphysical processes modulated the final PV modification by inducing PV production below regions of strong latent heat release within the WCB cloud (Fig. 6c). The negative PV change directly beneath the tropopause to the south of 56°N, behind the system's cold front, is associated with post-frontal convective activity. The region south of 56°N, between 312.5 K and 317.5 K, exhibits negligible θ change (Fig. 5a). Thus, this region of negative PV modification is constituted by air that travelled quasi-isentropically through regions of negative PV production induced by heating due to post-frontal convection (Fig. 6b) and radiative cooling at cloud top level (Fig. 6d). There is also a contribution from cloud microphysics (Fig. 6c) possibly induced by the heating produced by forced convection over the system's cold front to the south of the cyclone's center.

5. Diabatic effects in IOP14

Figure 7 shows θ_0 around the IOP14 cyclone center and the 2-PVU contours on two isentropic levels located at 320 K and 305 K to illustrate the synoptic situation at upper and lower levels, respectively. The intersection of the tropopause and the 320-K isentropic surface consists of a very distorted curve, as both tropospheric and stratospheric air masses have been stretched to form thin air strips spiraling into the cyclone's center (Fig. 7a). Just as in IOP13, the main feature on this level in terms of cross-isentropic ascent is the outflow of the system's WCB. The WCB typically splits into two distinct branches (Browning and Roberts 1994); the WCB split in IOP14 can be seen in Fig. 7a. One WCB branch turns anticyclonically, forming the primary WCB (WCB1, Browning and Roberts 1994). This branch undergoes strong cross-isentropic ascent as it is subject to strong heating (Martínez-Alvarado et al. 2014b). The second branch (WCB2) turns cyclonically wrapping around the cyclone's center (Browning and Roberts 1994). This branch undergoes relatively weaker cross-isentropic ascent than WCB1, as it is subject to less heating (Martínez-Alvarado et al. 2014b). In IOP14, there is a tropospheric air mass, located west of 20°W, which has experienced very strong cross-isentropic ascent originating from very low isentropic levels ($270 < \theta_0 < 310$ [K]). This air mass constitutes the system's WCB1 outflow. The system's WCB2 outflow consists of a distinct air mass that has undergone weaker cross-isentropic ascent, mainly originating within the layer $290 < \theta_0 < 320$ [K]. The dry intrusion in IOP14 consists of a long strip of stratospheric air that has been subject to weak cross-isentropic descent. IOP14 also exhibited low-level PV anomalies (Fig. 7b). These PV anomalies have a different structure to those in IOP13 (cf. Fig. 4b). Whereas IOP13 exhibited only one distinct low-level PV anomaly, IOP14 exhibits a series of low-level PV anomalies, forming a broken strip that spirals into the cyclone's center. Even though the cross-isentropic ascent and descent at lower levels are both weaker than at upper levels, the general spiral structure can also be easily discerned on the 305-K isentropic level.

Figure 8 shows θ_0, total diabatically-generated PV and 2-PVU contours on vertical sections along segment G–H in Fig. 7. Like segment E–F in Fig. 4, segment G–H is also a cross-section of the cyclone through its center, allowing a comparison between the two systems. Figure 9 shows the contributions to the modification of PV in IOP14 from the four parametrized processes considered here, as well as contours of PV = 2 PVU and θ to facilitate comparison with Figs. 7 and 8.

The cross-isentropic mass transport in IOP14 is much more complex than that in IOP13 (cf. Fig. 5a). Unlike IOP13, in which there was only one main column of strong cross-isentropic ascent, strong cross-isentropic as-

cent is ubiquitous throughout the cross section in IOP14. A comparison between the intersection of the columns of cross-isentropically ascending air on the 320-K isentropic level and the structures shown in Fig. 7 indicates that these columns are all part of the same air stream. This air stream corresponds to the system's WCB, whose secondary branch, WCB2, was tightly wrapped around the cyclone's center by this time. The highest column of cross-isentropic ascent (labelled C1 in Fig 8) is located around 54°N. Column C1 extends from around 800 hPa (300 K) up to near tropopause level, which in IOP14 by this time is located around 200 hPa (335 K). The diabatically-generated PV within this column is characterized by a core of positive diabatically-generated PV along the ascending axis over 54°N, extending from 900 hPa to around 380 hPa (Fig 8b). The core of positive PV is surrounded by negative diabatically-generated PV from 600 hPa to tropopause level (around 200 hPa). Column C1 is part of the WCB before the split; two smaller columns (labelled C2 and C3 in Fig 8), located south of 54°N, are part of WCB2. The column tops for columns C1 and C2 are also close to the local tropopause and their diabatically-generated PV structure resemble that of column C1's.

The air within the principal ascending branch of the system's WCB (column C1 in Fig. 8) produces similar patterns to those produced by the WCB in IOP13. BL processes are the main factor responsible for the negative PV production near tropopause level within this air stream (Fig. 9a). However, in this case the negative PV production is largely compensated by positive PV production due to the cloud microphysics parametrization (Fig. 9c), which indicates stronger heating due to this parametrization in IOP14 than in IOP13. Thus, the core of positive diabatically-generated PV over 54°N is formed by BL process at lower levels (below 500 hPa) and by cloud microphysical processes at upper levels (above 500 hPa). Dearden et al. (2015) have found, via independent simulations of this same case, that at these levels the heat released during vapor growth of ice within the WCB is a major factor in the creation of positive PV anomalies. The convection parametrization is a secondary contributor to the negative PV production at upper levels.

A column directly above the cyclone's center (labelled C4 in Fig 8) has a different structure to that of C1, C2 and C3 previously described. This column, characterised by high PV values which extend the 2-PVU contour from tropopause level to the surface, constitutes a PV tower (Rossa et al. 2000). The PV tower is the most prominent structure, exhibiting intense positive PV modification in its lower part (below 315 K) and negative PV modification in its upper part (Fig. 8b). A PV tower is typically composed of air from three different regions: tropopause-level air, low-level warm-sector air, and low-level cold-conveyor-belt air (Rossa et al. 2000). The air comprising each of these sources has a particular heating and PV modification history (Rossa et al. 2000).

The air from tropopause level exhibits negligible θ change, i.e this air has travelled quasi-isentropically, experiencing weak PV reduction along its path. Parametrized processes contribute small negative PV modification to make up the total negative diabatically-generated PV (especially noticeable around 275 hPa in Fig. 8b).

The warm-sector air has undergone cross-isentropic ascent mainly as a result of heating and mixing within the BL, but with contribution from the convection parametrization. As the air ascended cross-isentropically through the BL, the cloud microphysics parametrization produced a small negative contribution to the θ change (not shown). The positive PV change is driven by BL and turbulent mixing processes (Fig. 9a) and heating due to the convection parametrization (Fig. 9b). However, there is also a negative contribution induced by radiative cooling taking place in clouds at BL top level (Fig. 9d). The air moving within the system's cold conveyor belt into the PV tower, being drier and colder than that from the warm sector, also experiences less cross-isentropic ascent than the warm-sector air. Like for the warm-sector air, BL and mixing processes drive cross-isentropic ascent, while cloud microphysics tends to counteract this ascent by cooling the air as it ascends cross-isentropically through the BL. However, the magnitude of BL heating is weaker in the cold-conveyor-belt air than in the warm-sector air. Another important difference between the history of the warm-sector air and that of the cold-conveyor-belt air is given by the contribution from the convection parametrization, which in the latter is negligible. The PV increased as the cold-conveyor-belt air within the PV tower travelled through regions of PV production induced by heating due to cloud microphysical processes (Fig. 9c). However, this air also travelled through regions of negative PV production induced by BL and mixing processes (Fig. 9a) and regions of positive then negative PV production induced by the convection parametrization (Fig. 9b).

6. Cyclone comparison

The results presented so far are restricted to the selected horizontal and vertical sections. A more thorough comparison is achieved by the integral diagnostics within areas around the location of the cyclones under comparison. The results from such integral diagnostics, formulated around the diabatic tracers are presented in the following two sections.

a. Cross-isentropic mass transport

In this section θ_0 distributions are computed following the method described in Section 2d. The results are shown in Fig. 10, in which each color segment represents a θ_0-bin.

There are three lines for each color segment. These lines represent the 2.5^{th} (dashed), 50^{th} (bold) and 97.5^{th} (thin) percentiles in each θ_0-bin as functions of time. These percentiles are used to describe the evolution of each θ_0 distribution. Figure 10a shows the results for IOP13; Fig. 10b shows the results for IOP14. The medians illustrate the strong stratification expected when averaging over these length scales ($\mathcal{O}(1000$ km)).

The minimum θ value in each cyclone illustrate a major difference between the environments of these cyclones: IOP13 evolves in an environment around 10 K colder than does IOP14, which also implies the potential for greater moisture availability near the surface in IOP14. The location of the 2.5th and 97.5th percentiles essentially determine the range of the θ_0 distributions. There are layers in both cyclones that are largely isentropic, for which the 2.5th and 97.5th percentiles are flat. These are located at upper levels, above 320 K in IOP13 and above 330 K in IOP14, corresponding to stratospheric layers. The difference in the vertical locations of these largely isentropic layers is consistent with the differences in tropopause height suggested by the vertical sections in Figs. 5 and 8. The most important differences between the cyclones are described by the 97.5th-percentile lines. Both cyclones exhibit a certain degree of cross-isentropic ascent throughout the 21-h period. However, while in IOP13 such ascent is gradual and noticeable only in the layers away from the lower boundary ($\theta_0 > 290$ K), in IOP14 the cross-isentropic ascent is more intense and spans the whole troposphere from the surface up to the tropopause.

Figures 10(c, d) show θ changes for the bin $300 < \theta_0 \leq 310$ [K] (cyan lines in Fig. 10) in IOP13 and IOP14, respectively. The emergent structure is similar in both cases with the band top showing layers of increasing heating. However, the heating intensity is very different between the two cases. In IOP13 the heating attains a maximum near the end of the 21-h period barely reaching 10 K. In contrast, heating between 15 K and 20 K is reached in less than 10 hours into the simulation in IOP14.

Figure 11 shows the contributions to the θ changes in Figs. 10(c,d) from the four parametrized processes considered here. The BL and turbulent mixing parametrization is the main contributor in both cases (Fig. 11(a,e)). The convection parametrization starts contributing about five hours earlier in IOP14 than in IOP13 (Fig. 11(b,f)). Furthermore, this parametrization acts on a much wider layer in IOP14 than in IOP13, spanning from the 75th percentile up. This is consistent with the differences between cases in terms of convective activity, as described in Sections 4 and 5. The cloud microphysics parametrization in IOP14 starts contributing about two hours later than the convection parametrization in IOP14, but about nine hours earlier than the cloud microphysics parametrization in IOP13 (Fig. 11(c,g)). In the atmosphere, like in a numerical model, the main source of heating are water phase changes. Despite the inter-case differences, this fact is highlighted by both cases: The three parametrization schemes that contribute to total heating do so mainly through latent heat release, including the BL and turbulent mixing parametrization. The latent heat release associated with the latter scheme can be found by tracing the changes in cloud liquid water and associated θ changes due to this parametrization (Martínez-Alvarado and Plant 2014). In the atmosphere, unlike in a numerical model, phase changes are not distributed among parametrization schemes and the challenge for numerical models is to achieve the actual heating and induced cross-isentropic mass transport through the interaction between parametrization schemes and between the parametrization schemes and the dynamical core. These aspects are not always well represented by current numerical models (e.g. Martínez-Alvarado et al. 2015).

In general, the 2.5th-percentile lines in Fig. 10 describe mild cross-isentropic subsidence in both cyclones, corresponding to the widespread cross-isentropic subsidence discussed in Sections 4 and 5. This subsidence is associated with cooling. Figures 10(c,d) show that the lower part of the band with $300 < \theta_0 \leq 310$ [K] exhibits relatively weak cooling towards the end of the 21-h period in both cases. However, the cooling starts much earlier in IOP14 than in IOP13. The main parametrized process that contributes to cooling in IOP13 is radiation (Fig. 11d), but convection and cloud microphysics also contribute. In comparison, there are only two processes that contribute to cooling in IOP14, namely cloud microphysics (Fig. 11g) and radiation (Fig. 11h). Both processes have a relatively larger effect and over a wider layer in IOP14 than in IOP13.

b. Circulation

In this section we follow the method described in Section 2e to compute the area-averaged isentropic vorticity ζ_θ and the contributions to ζ_θ associated with the materially-conserved and the diabatically-generated PV, $\zeta_{\theta,0}$ and $\zeta_{\theta,\mathrm{d}}$. The latter two are computed as

$$\zeta_{\theta,0} = \frac{1}{A}\int_R \sigma\, Q_0 dx\, dy \quad \text{and} \quad \zeta_{\theta,\mathrm{d}} = \frac{1}{A}\int_R \sigma\, Q_\mathrm{d} dx\, dy, \tag{18}$$

where $A = \int_R dx\, dy$.

When a large integration region (~ 1000 km) is used, the cyclones have similar vertical structures, an effect that has been noted in previous studies (Čampa and Wernli 2012). When this is done for IOP13 and IOP14 (not shown), the ζ_θ profile is almost constant vertically in both cases, corresponding to $\zeta_\theta \simeq 1.16f$ and $\zeta_\theta \simeq 1.25f$ in IOP13 and IOP14, respectively. This shows that, when these large length scales are considered, not only are the cyclones very similar to each other, but also the values of ζ_θ are very close

to the value that ζ_θ would have in an unperturbed atmosphere. Furthermore, the diabatic processes' contribution is small in both cases, apart from a low-level enhancement below 600 hPa in IOP14.

When smaller length scales are considered, the differences between cyclones are more apparent. Figure 12 shows the results corresponding to the last 18 hours in each simulation using, as integration regions, 500-km radius circles concentric to each cyclone at each time. The figure shows ζ_θ (black lines), the contribution from the materially-conserved PV (blue lines) and the total contribution from diabatic PV (orange lines) in IOP13 (upper row) and IOP14 (lower row). To provide an estimate of uncertainty due to the residual tracer r_Q, its contribution, computed as $\zeta_{\theta,\mathrm{r}} = \zeta_\theta - (\zeta_{\theta,0} + \zeta_{\theta,\mathrm{d}})$, has been added and subtracted from the conserved and diabatic tracers (dashed lines). The value of planetary vorticity, f, at the position of the cyclone's center (grey lines) is also shown. All the computations have been carried out on isentropic surfaces, but to ease interpretation the results are also shown in isobaric coordinates. The indicated pressures correspond to the average pressure within the integration region at each isentropic level.

The IOP13 cyclone developed in a weakly cyclonic environment ($\zeta_\theta \simeq f$ at the start of the simulation; not shown). After three hours into the simulation ζ_θ is approximately vertically constant with height and $\zeta_\theta \simeq 1.20f$ (Fig. 12a). As time passes, the ζ_θ profile remains constant up to around 500 hPa, level above which the ζ_θ values tend to increase due to the enhanced presence of stratospheric air. Below the 500-hPa level ζ_θ increases slowly to reach a value at the end of the 21-h simulation of $\zeta_\theta \simeq 1.33f$ (Fig. 12d). This value is 15% larger than the value found when using a 1000-km radius circle as integration region. The diabatic contributions to the ζ_θ vertical profile in IOP13 developed over the first 15 hours of the simulation, which corresponds to 0300 UTC 18 July 2012 (Fig. 12c), after which a final state profile can be recognized. Positive diabatic contributions became important in the layer $450 < p < 650$ [hPa] (Fig. 12b) after the first nine hours of the simulation. Positive diabatic contributions then spread from that layer to lower levels, developing into a uniform contribution (Fig. 12c). Negative diabatic contributions are found at levels above 450 hPa, especially after the first fifteen hours of the simulation (Fig. 12c).

In contrast, the IOP14 cyclone developed in an already highly cyclonic environment ($\zeta_\theta > f$ at the start of the simulation), preconditioned by the presence of other low pressure systems in that same area (not shown). Thus, at the beginning of the 21-h study period ζ_θ was already large at mid-tropospheric levels. Three hours into the simulation the ζ_θ vertical profile is stratified into two layers (Fig. 12e). The lower layer (below 600 hPa) is characterized by $\zeta_\theta \simeq 1.47f$. Above 600 hPa, ζ_θ gradually increases with height to almost twice the value of the planetary vorticity ($\zeta_\theta \simeq 1.87f$) around 500 hPa. This early profile then evolved during the following 18 hours into an approximately constant vertical profile with $\zeta_\theta \simeq 1.87f$ throughout (Fig. 12h). This value is 50% larger than the value found when using a 1000-km radius circle as isentropic integration area. In contrast to IOP13, the diabatic contributions to the ζ_θ vertical profile in IOP14 developed very rapidly, during the first nine hours of the simulation, into a final profile that only changed in intensity (Fig. 12f–h). Negative diabatic contributions were restricted to the layer $470 < p < 580$ [hPa]. Both, above and below that layer, diabatic processes contributed positively to ζ_θ. However, only in the lower layer the diabatic positive contributions clearly increased with time.

A general property of the diabatic PV tracers is that the gain in the contribution due to diabatic processes across a given isentropic surface will always be balanced by a loss in the contribution due to the Q_0 tracer and vice versa, except where the isentropic surface intersects orography. This property can be demonstrated as follows. In isentropic coordinates, Q_0 and Q_d satisfy the following equations:

$$\frac{DQ_0}{Dt} = 0 \quad \text{and} \quad \frac{DQ_\mathrm{d}}{Dt} = -\frac{1}{\sigma}\nabla_\theta \cdot \boldsymbol{\mathcal{J}}_{\boldsymbol{F},\dot{\theta}}, \tag{19}$$

where $\nabla_\theta = (\partial_x, \partial_y, \partial_\theta)$ is the gradient in isentropic coordinates and

$$\boldsymbol{\mathcal{J}}_{\boldsymbol{F},\dot{\theta}} = \left(\frac{\partial\theta}{\partial z}\right)^{-1} \boldsymbol{J}_{\boldsymbol{F},\dot{\theta}}, \tag{20}$$

where $\boldsymbol{J}_{\boldsymbol{F},\dot{\theta}} = -\dot{\theta}\,\nabla \times \boldsymbol{u} - \boldsymbol{F} \times \nabla\theta$ is the part of the PV flux associated with the material rate of change of θ, $\dot{\theta} = D\theta/Dt$, and the frictional or other arbitrary force per unit mass exerted on the air, $\boldsymbol{F}$.

Using (19), the flux form of the PV equation (e.g. Haynes and McIntyre 1987)

$$\frac{\partial(\sigma Q)}{\partial t} + \nabla_\theta \cdot \boldsymbol{\mathcal{J}} = 0 \tag{21}$$

can be split into two parts:

$$\frac{\partial(\sigma Q_0)}{\partial t} + \nabla_\theta \cdot \boldsymbol{\mathcal{J}}_0 = 0 \quad \text{and} \quad \frac{\partial(\sigma Q_\mathrm{d})}{\partial t} + \nabla_\theta \cdot \boldsymbol{\mathcal{J}}_\mathrm{d} = 0, \tag{22}$$

where

$$\boldsymbol{\mathcal{J}}_0 = \sigma Q_0 \boldsymbol{v}_\theta \quad \text{and} \quad \boldsymbol{\mathcal{J}}_\mathrm{d} = \sigma Q_\mathrm{d} \boldsymbol{v}_\theta + \boldsymbol{\mathcal{J}}_{\boldsymbol{F},\dot{\theta}}, \tag{23}$$

$\boldsymbol{v}_\theta = (u, v, \dot{\theta})$ is the three-dimensional wind velocity in isentropic coordinates and

$$\boldsymbol{\mathcal{J}} = \boldsymbol{\mathcal{J}}_0 + \boldsymbol{\mathcal{J}}_\mathrm{d}. \tag{24}$$

Haynes and McIntyre (1987) showed that the flux $\boldsymbol{\mathcal{J}}$ always lies on isentropic surfaces, i.e. its cross-isentropic component $\mathcal{J} = 0$. In contrast, the fluxes in (23) do not lie on

isentropic surfaces unless the motion is adiabatic. Their cross-isentropic components are given by

$$\mathcal{J}_0 = \sigma Q_0 \dot{\theta}, \tag{25}$$

and

$$\mathcal{J}_\mathrm{d} = \sigma Q_\mathrm{d} \dot{\theta} + \mathcal{J}_{\boldsymbol{F},\dot{\theta}}. \tag{26}$$

Equation (25) makes the influence of diabatic processes on the evolution of Q_0 explicit. Under adiabatic conditions Q_0 will be simply redistributed isentropically. Since the cross-isentropic component of (24) is zero, we have that

$$\mathcal{J}_{\boldsymbol{F},\dot{\theta}} = -\sigma Q \dot{\theta}. \tag{27}$$

According to (27), Q_d can still be modified by frictional forces under adiabatic conditions, but no cross-isentropic flux would take place. Substituting (27) into (26) yields

$$\mathcal{J}_\mathrm{d} = -\sigma Q_0 \dot{\theta} = -\mathcal{J}_0, \tag{28}$$

i.e. the cross-isentropic advection of Q_d is equal in magnitude, but opposite in sign to that of Q_0, just as it should be for Q to satisfy the PV impermeability theorem (Haynes and McIntyre 1987). This property partially explains the patterns observed in Fig. 12, in which a change in the contribution from $\zeta_{\theta,\mathrm{d}}$ at a given isentropic level is approximately balanced by the opposite change in the contribution due to $\zeta_{\theta,0}$ w.r.t. ζ_θ. However, the total variation of ζ_θ on a given layer is determined not only through this effect, but also by the isentropic advection of Q_0 and Q_d and the effects of frictional forces and diabatic processes, as given by the isentropic components of the vectors in (24). While the vertical profile of ζ_θ in IOP13 remains approximately invariant in time for most of the considered period, the corresponding profile in IOP14 changes throughout. Thus, in IOP13 the net PV flux of across the integration region's boundary is small, which implies that the net flux of Q_d almost exactly balances the net flux of Q_0 into the integration region. In contrast, in IOP14 the net flux of Q_d across the integration region's boundary is not balanced by the net flux of Q_0, which leads to a net change in ζ_θ.

Figure 13 shows the contributions from individual diabatic processes to the ζ_θ vertical profiles. Figures 13(a–d) show the evolution of these contributions in IOP13; Figs. 13(e–h) show the corresponding evolution in IOP14. The two cases exhibit some similarities. In both cases, the BL and turbulent mixing parametrization produces a strong positive contribution at low levels and a strong negative contribution at upper levels. This effect is consistent with the discussion in Sections 4 and 5, regarding a heating maximum due to the BL and turbulent mixing parametrization around the level of BL top, which induces positive PV modification underneath and negative PV modification above. Also in both cases, the cloud microphysics parametrization produces an almost opposite pattern to the pattern produced by the BL and turbulent mixing parametrization: a neutral to negative contribution at low levels and a strong positive contribution at upper levels. However, the similarities are far exceeded by the dissimilarities. The vertical location and span of the contributions due to the BL and the cloud microphysics parametrization schemes largely depend on the case. The most important difference in location and span is found in the contribution due to the cloud microphysics parametrization. This contribution is largest above the 600-hPa level in IOP13 (Figs. 13(a–d)) while in IOP14 this contribution tends to be more uniform throughout the layer shown in the figure. Another important difference between IOP13 and IOP14 is due to the contribution from the convection parametrization. This contribution is very small in IOP13 and only becomes noticeable above 500 hPa after 0300 UTC 18 July (Fig. 13b). Above that level, this contribution is negative and consistent with the region of negative PV modification discussed in Section 4 (cf. Fig. 6b). In contrast, the contribution due to the convection parametrization is important even from the beginning of the simulation in IOP14 (Figs. 13(e–h)). This contribution determines important features such as the location and intensity of the diabatically-generated PV contribution in the layer of where this is negative ($470 < p < 580$ [hPa], cf. Figs. 12(e–h)). Below that layer, the positive contribution is due to the BL and cloud microphysics parametrization schemes.

7. Summary and conclusions

Two extratropical cyclones that occurred during summer 2012 have been analyzed. Despite similarities in precipitation and cyclone stationarity, the cyclones represented very different synoptic conditions. The first cyclone, observed during the DIAMET IOP13, was a typical summer cyclone, which deepened down to 995 hPa. In contrast, the second cyclone, observed during the IOP14, was a much deeper cyclone, with a minimal central pressure of 978 hPa. The analysis was performed through simulations performed with the MetUM enhanced with diabatic tracers of θ and PV. The simulations were compared with radar rainfall observations and dropsonde measurements. The large-scale environment was represented well by the model in both cases (Fig. 1). Furthermore, despite differences caused mainly by a systematic wet bias in the model, the simulations provided a good representation of the mesoscale structure for at least 21 hours for IOP13 and 22 hours for IOP14 (Figs. 2–3).

The environment during IOP13 was colder and, therefore, drier than the environment during IOP14. These contrasting environmental conditions led to weaker diabatic effects during IOP13 than during IOP14. The cyclone during IOP13 was characterized by a single column of large-scale ascent, corresponding to the system's WCB, and weak low-

level positive PV anomalies (Figs. 4 and 5a). In contrast, the cyclone during IOP14 was characterized by a powerful WCB that wrapped in a spiral around the cyclone's center forming several columns of large-scale ascended air (Figs. 7 and 8a). Furthermore, this cyclone exhibited very strong positive PV anomalies, extending throughout the troposphere and constituting a PV tower. In both cases, the low-level positive PV anomalies were diabatically produced (Figs. 5b and 8b). However, the amount of diabatic activity and the contribution from different parametrized processes were different in each case. In IOP13 the processes that contributed the most to the production of the low-level positive PV anomaly were the BL and turbulent mixing and cloud microphysics parametrization schemes (Fig. 6). In addition to these two processes, the convection parametrization also contributed to the production of the low-level positive PV anomaly in IOP14 (Fig. 9).

The materially-conserved tracer θ_0 was used to label air masses for the analysis of cross-isentropic motion around the cyclones' centers. This analysis revealed striking differences in the cross-isentropic motion taking place in each cyclone. In IOP13 this motion was gradual and mainly affected the layers in the middle part of the troposphere (Fig. 10(a,c)). In contrast, in IOP14 cross-isentropic motion was stronger and virtually affected the whole troposphere (Fig. 10(b,d)). In both cases, heating was primarily produced by latent heat release through three parametrization schemes, namely BL and turbulent mixing, convection and cloud microphysics (Fig. 11). In both cases, the BL and turbulent mixing parametrization was the main contributor to total heating. However, the contribution from the BL and turbulent mixing scheme in IOP14 was 50% stronger than in IOP13. Furthermore, the convection parametrization contributed for longer and over a wider layer in IOP14 than in IOP13, confirming the importance of the convection parametrization in the development of the cyclone in IOP14. The radiation scheme mainly produced cooling in both cyclones. However, the magnitude of the radiation contribution was larger and affected a deeper layer in IOP14 than in IOP13. Stronger radiative cooling as well as stronger cooling due to cloud microphysics processes led to stronger cross-isentropic subsidence in IOP14 than in IOP13.

The use of the integral interpretation of diabatically-generated PV tracers in terms of ζ_θ enabled the assessment of the effects of diabatic processes on the circulation around the cyclone center. When the integration was carried out over a large area (~ 1000 km) the cyclones exhibited similar characteristics despite being very different systems: $\zeta_\theta \simeq f$ throughout the troposphere and small diabatic contribution in both cases. However, when the analysis was performed over smaller integration areas (~ 500 km), the differences between the cyclones became more apparent. One important difference between the cyclones is that while the vertical profile of ζ_θ in IOP13 remains approximately invariant in time for most of the considered period (Figs. 12(a–d)), the corresponding profile in IOP14 changes throughout (Figs. 12(e–h)). Using the properties of PV tracers, it was shown that in IOP13 the time-invariance of the ζ_θ profile was achieved through the cancellation of the net flux of diabatically-generated PV into the integration region by that associated with the materially-conserved PV. It was shown that in the cross-isentropic direction, the PV impermeability theorem (Haynes and McIntyre 1987) implies this cancellation. However, in the isentropic direction, the balance between the fluxes of Q_0 and Q_d depends on the cyclone's particular dynamical conditions. Thus, in IOP14 the changes in the vertical profile of ζ_θ with time are due to the isentropic advection of both Q_d and Q_0 as well as the effects of frictional forces and diabatic processes into the integration region.

Finally, despite differences between both cyclones in terms of the contributions of every individual parametrized process to total PV, the main difference occurred in the contribution from the convection parametrization. This contribution was very small in IOP13 (Figs.13(a–d)) while it is important from the beginning of the simulation in IOP14 (Fig.13(e–h)).

The analysis of these two contrasting summer cyclones has shown the suitability of diabatic θ and PV tracers, especially under their integral interpretations, for the analysis of diabatic effects. One important property of these interpretations is that the tracers effectively become independent of model resolution. A potential use of this property is the assessment of consistency between simulations at different resolutions, which is essential to achieve, for example, truly seamless numerical models.

Acknowledgments.

This work was initiated by the MSc dissertation of Ms Na Zhou, supervised by Profs Gray and Methven at the Department of Meteorology, University of Reading, and was funded by the United Kingdom's Natural Environment Research Council (NERC) as part of the DIAMET project (NE/I005234/1). We thank Dr Jeffrey Chagnon, for useful discussion during the initial development of this work and, together with Mr Leo Saffin, for the implementation of PV tracers into the MetUM; Dr Christopher Dearden, for useful comments to the initial manuscript; the Met Office, for making the MetUM and associated initial and lateral boundary condition files available, and the NERC-funded National Centre for Atmospheric Science–Computational Modelling Services, for providing computing and technical support. The BAe-146 aircraft was flown by Directflight Ltd and managed by FAAM on behalf of NERC and the Met Office.

REFERENCES

Adler, R., et al., 2003: The version 2 Global Precipitation Climatology Project (GPCP) monthly precipitation analysis (1979-present). *J. Hydrometeorol.*, **4**, 1147–1167.

Arakawa, A. and V. Lamb, 1977: Computational design of the basic dynamical processes of the UCLA General Circulation Model. *Methods Comput. Phys.*, **17**, 173–265.

Browning, K. A. and N. M. Roberts, 1994: Structure of a frontal cyclone. *Q. J. R. Meteorol. Soc.*, **120**, 1535–1557.

Čampa, J. and H. Wernli, 2012: A PV perspective on the vertical structure of mature midlatitude cyclones in the Northern Hemisphere. *J. Atmos. Sci.*, **69**, 725–740.

Chagnon, J. M. and S. L. Gray, 2009: Horizontal potential vorticity dipoles on the convective storm scale. *Q. J. R. Meteorol. Soc.*, **135**, 1392–1408.

Chagnon, J. M. and S. L. Gray, 2015: A diabatically-generated potential vorticity structure near the extratropical tropopause in three simulated extratropical cyclones. *Mon. Weather Rev.*, **143**, 2337–2347, doi:10.1175/MWR-D-14-00092.1.

Chagnon, J. M., S. L. Gray, and J. Methven, 2013: Diabatic processes modifying potential vorticity in a North Atlantic cyclone. *Q. J. R. Meteorol. Soc.*, **139**, 1270–1282.

Charney, J. G. and N. A. Phillips, 1953: Numerical integration of the quasi-geostrophic equations for barotropic and simple baroclinic flows. *J. Meteor.*, **10 (2)**, 71–99.

Davies, T., M. J. P. Cullen, A. J. Malcolm, M. H. Mawson, A. Staniforth, A. A. White, and N. Wood, 2005: A new dynamical core for the Met Office's global and regional modelling of the atmosphere. *Q. J. R. Meteorol. Soc.*, **131**, 1759–1782.

Dearden, C., G. Vaughan, T. Tsai, and J. P. Chen, 2015: Exploring the diabatic role of ice microphysical processes in UK summer cyclones. *Mon. Weather Rev.*, submitted.

Dee, D. P., et al., 2011: The era-interim reanalysis: configuration and performance of the data assimilation system. *Q. J. R. Meteorol. Soc.*, **137**, 553–597.

Edwards, J. and A. Slingo, 1996: Studies with a flexible new radiation code. Part I: Choosing a configuration for a large-scale model. *Q. J. R. Meteorol. Soc.*, **122**, 689–719.

Gray, S. L., 2006: Mechanisms of midlatitude cross-tropopause transport using a potential vorticity budget approach. *J. Geophys. Res.*, **111 (D17113)**, 14 pp, doi:10.1029/2005JD006259.

Gregory, D. and P. R. Rowntree, 1990: A mass flux convection scheme with representation of cloud ensemble characteristics and stability-dependent closure. *Mon. Weather Rev.*, **118**, 1483–1506.

Hawcroft, M. K., L. C. Shaffrey, K. I. Hodges, and H. F. Dacre, 2012: How much northern hemisphere precipitation is associated with extratropical cyclones? *Geophys. Res. Lett.*, **39**, L24809.

Haynes, J. M., T. H. Vonder Haar, T. L'Ecuyer, and D. Henderson, 2013: Radiative heating characteristics of earth's cloudy atmosphere from vertically resolved active sensors. *Geophys. Res. Lett.*, **40**, 624–630.

Haynes, P. H. and M. E. McIntyre, 1987: On the evolution of vorticity and potential vorticity in the presence of diabatic heating and frictional or other forces. *J. Atmos. Sci.*, **44**, 828–841.

Huffman, G. J., R. F. Adler, M. M. Morrissey, D. T. Bolvin, S. Curtis, R. Joyce, B. McGavock, and J. Susskind, 2001: Global precipitation at one-degree daily resolution from multisatellite observations. *J. Hydrometeorol.*, **2**, 36–50.

Klocke, D. and M. Rodwell, 2013: A comparison of two numerical weather prediction methods for diagnosing fast-physics errors in climate models. *Q. J. R. Meteorol. Soc.*, in Press.

Lock, A. P., A. R. Brown, M. R. Bush, G. M. Martin, and R. N. B. Smith, 2000: A new boundary layer mixing scheme. Part I: Scheme description and single-column model tests. *Mon. Weather Rev*, **128**, 3187–3199.

Martínez-Alvarado, O., L. H. Baker, S. L. Gray, J. Methven, and R. S. Plant, 2014a: Distinguishing the cold conveyor belt and sting jet air streams in an intense extratropical cyclone. *Mon. Weather Rev.*, **142**, 2571–2595.

Martínez-Alvarado, O., H. Joos, J. Chagnon, M. Boettcher, S. L. Gray, R. S. Plant, J. Methven, and H. Wernli, 2014b: The dichotomous structure of the warm conveyor belt. *Q. J. R. Meteorol. Soc.*, **140**, 1809–1824, doi:10.1002/qj.2276.

Martínez-Alvarado, O., E. Madonna, S. L. Gray, and H. Joos, 2015: A route to systematic error in forecasts of Rossby waves. *Q. J. R. Meteorol. Soc.*, in press.

Martínez-Alvarado, O. and R. S. Plant, 2014: Parameterised diabatic processes in numerical simulations of an extratropical cyclone. *Q. J. R. Meteorol. Soc.*, **140**, 1742–1755, doi:10.1002/qj.2254.

Rossa, A. M., H. Wernli, and H. C. Davies, 2000: Growth and decay of an extra-tropical cyclone's PV-tower. *Meteorol. Atmos. Phys.*, 139–156.

Schäfler, A. and F. Harnisch, 2015: Impact of the inflow moisture on the evolution of a warm conveyor belt. *Q. J. R. Meteorol. Soc.*, **141**, 299–310.

Simmons, A. J., S. Uppala, D. Dee, and S. Kobayashi, 2007: ERA-Interim: New ECMWF reanalysis products from 1989 onwards. *ECMWF Newsletter*, **110**, 25–35.

Stoelinga, M. T., 1996: A potential vorticity-based study of the role of diabatic heating and friction in a numerically simulated baroclinic cyclone. *Mon. Weather Rev.*, **124**, 849–874.

Vaughan, G., et al., 2015: Cloud banding and winds in intense European cyclones – Results from the DIAMET Project. *B. Am. Meteorol. Soc.*, **96**, 249–265.

Whitehead, J. P., C. Jablonowski, J. Kent, and R. B. Rood, 2014: Potential vorticity: measuring consistency between GCM dynamical cores and tracer advection schemes. *Q. J. R. Meteorol. Soc.*, in Press.

Wilson, D. R. and S. P. Ballard, 1999: A microphysically based precipitation scheme for the UK Meteorological Office Unified Model. *Q. J. R. Meteorol. Soc.*, **125**, 1607–1636.

Zhu, Y. and R. E. Newell, 1998: A proposed algorithm for moisture fluxes from atmospheric rivers. *Mon. Weather Rev.*, **126**, 725–735.

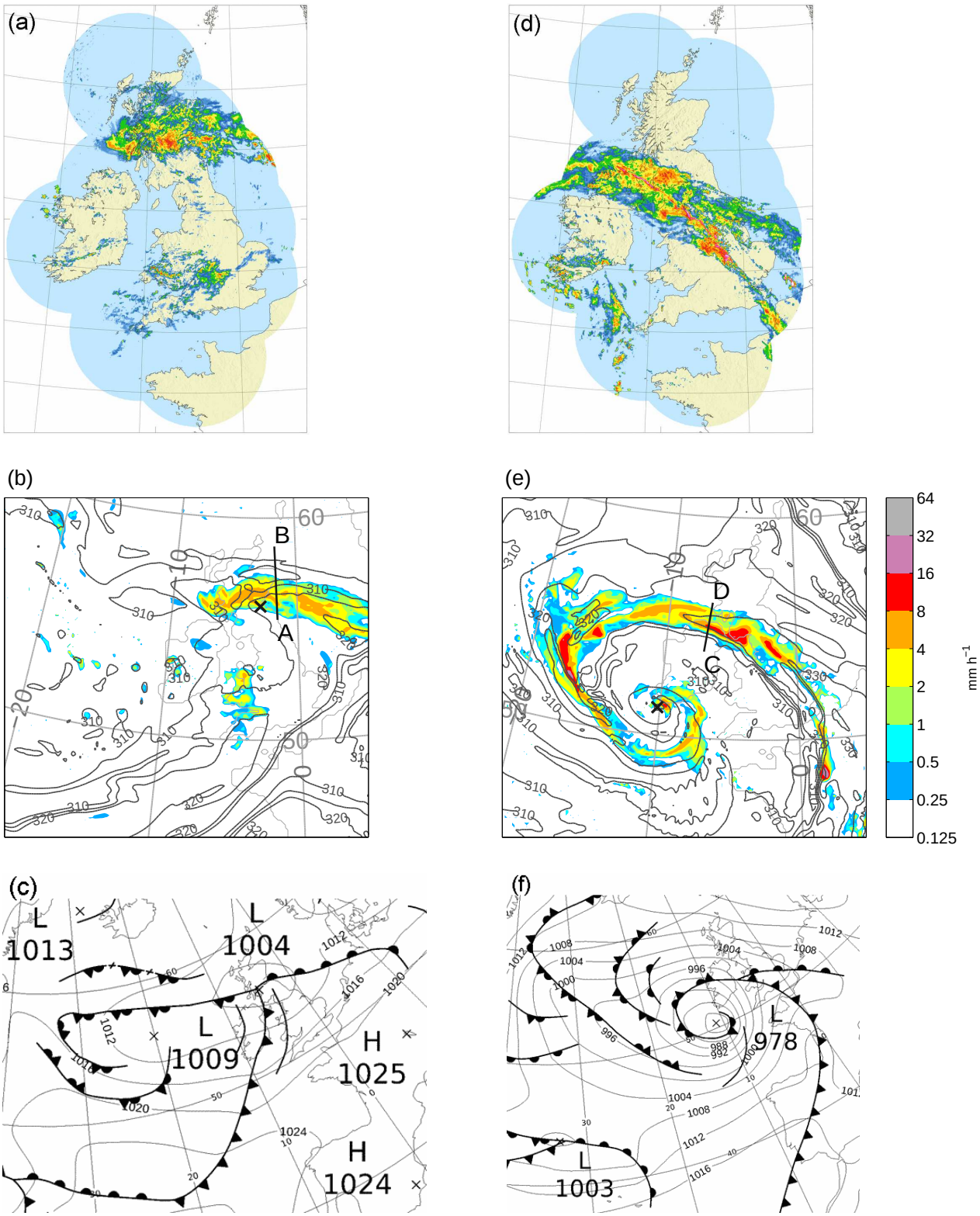

Figure 1: (a,d) Radar rainfall rates (courtesy Met Office ©2012 Crown Copyright) and (b,e) model-derived rainfall rates at (a,b) 0900 UTC 18 July 2012 and (d,e) 1500 UTC 15 August 2012 . In (b,e), thin lines represent contours of 850-hPa equivalent potential temperature, in K and with a separation of 5 K, and the bold X represents the position of the low-pressure center while the segments A–B and C–D indicate the approximate position of dropsonde curtains. Synoptic charts at (c) 0600 UTC 18 July 2012 and (f) 1200 UTC 15 August 2012 (courtesy Met Office ©2012 Crown Copyright).

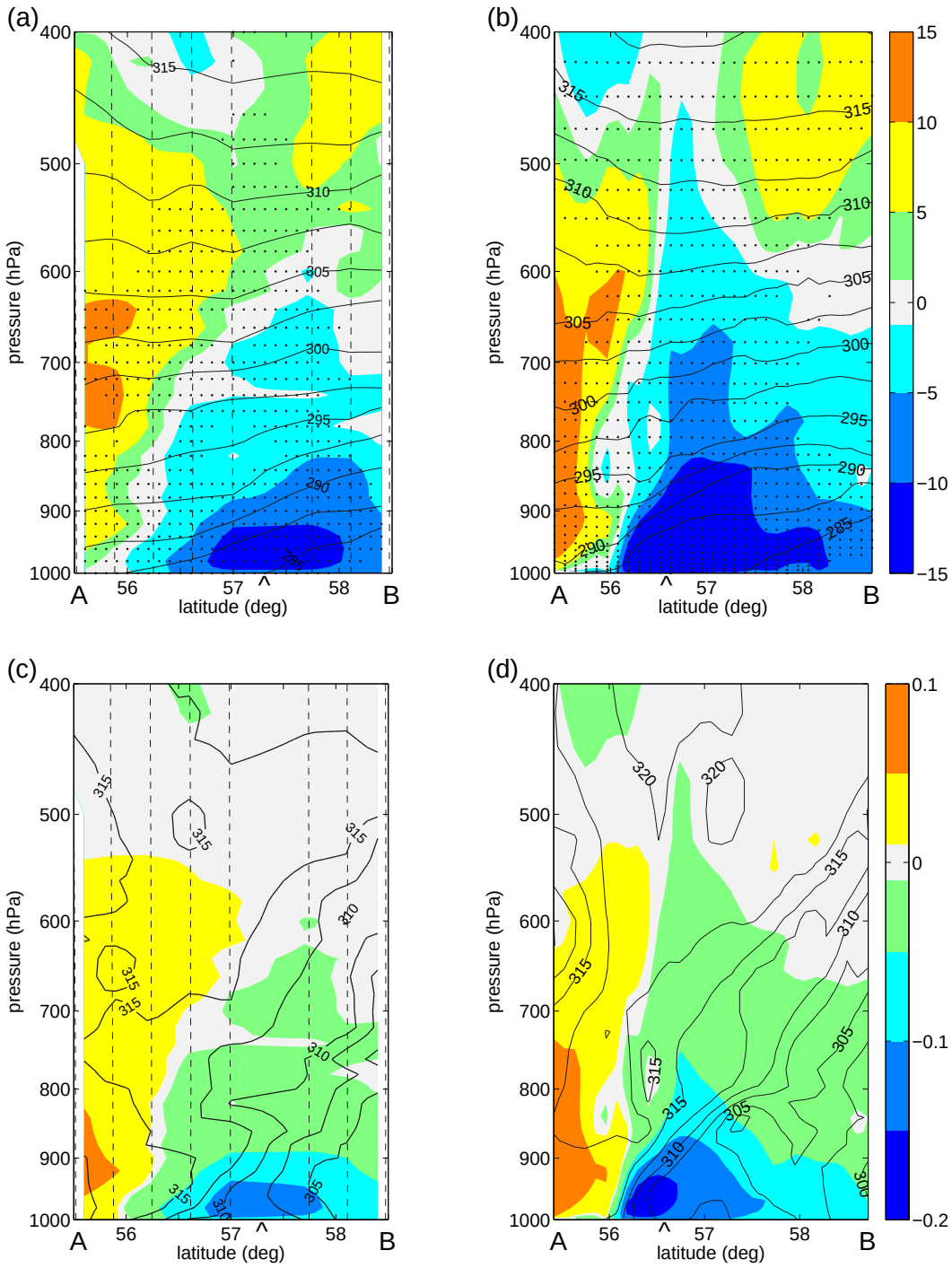

Figure 2: Vertical section along segment A–B in Fig. 1b showing in color shading **(a,b)** zonal velocity, in m s^{-1}, and **(c,d)** water vapor flux, in kg m^{-2} s^{-1}, at 0900 UTC 18 July 2012 (IOP13) derived from **(a,c)** dropsonde observations and **(b,d)** model output. In **(a,b)**, thin black lines represent potential temperature, in K, with a separation of 2.5 K; stippled areas indicate areas where relative humidity w.r.t. ice is larger than 90%. In **(c,d)**, thin black lines represent equivalent potential temperature contours, in K, with a separation of 2.5 K. Thin dashed lines in **(a,c)** represent dropsonde paths. The wedges mark the position of the 900-hPa front.

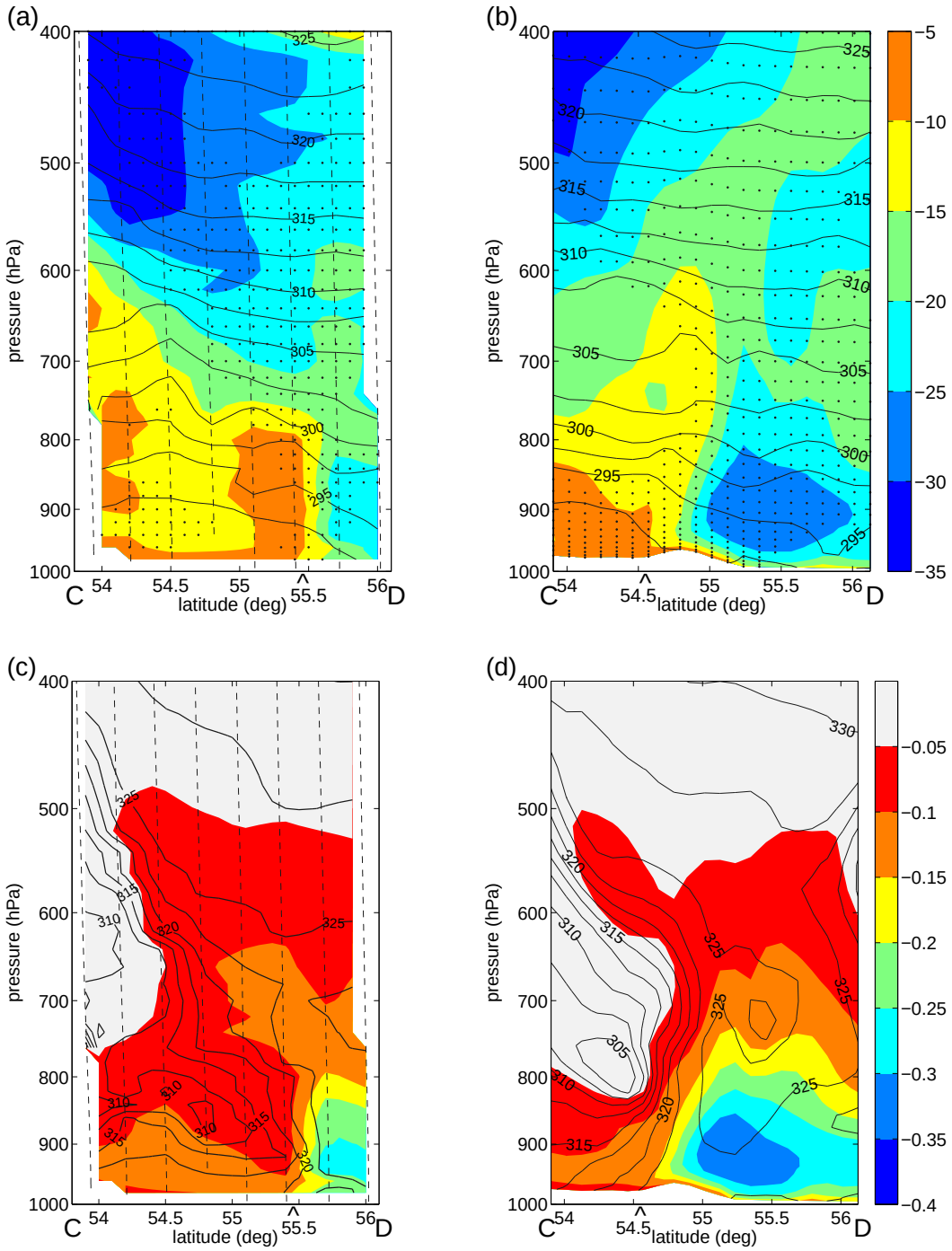

Figure 3: Vertical section along segment C–D in Fig. 1e showing in color shading **(a,b)** zonal velocity, in m s^{-1}, and **(c,d)** water vapor flux, in kg m^{-2} s^{-1}, at 1600 UTC 15 August 2012 (IOP14) derived from **(a,c)** dropsonde observations and **(b,d)** model output. In **(a,b)**, thin black lines represent potential temperature, in K, with a separation of 2.5 K; stippled areas indicate areas where relative humidity w.r.t. ice is larger than 90%. In **(c,d)**, thin black lines represent equivalent potential temperature contours, in K, with a separation of 2.5 K. Thin dashed lines in **(a,c)** represent dropsonde paths. The wedges mark the position of the 900-hPa front.

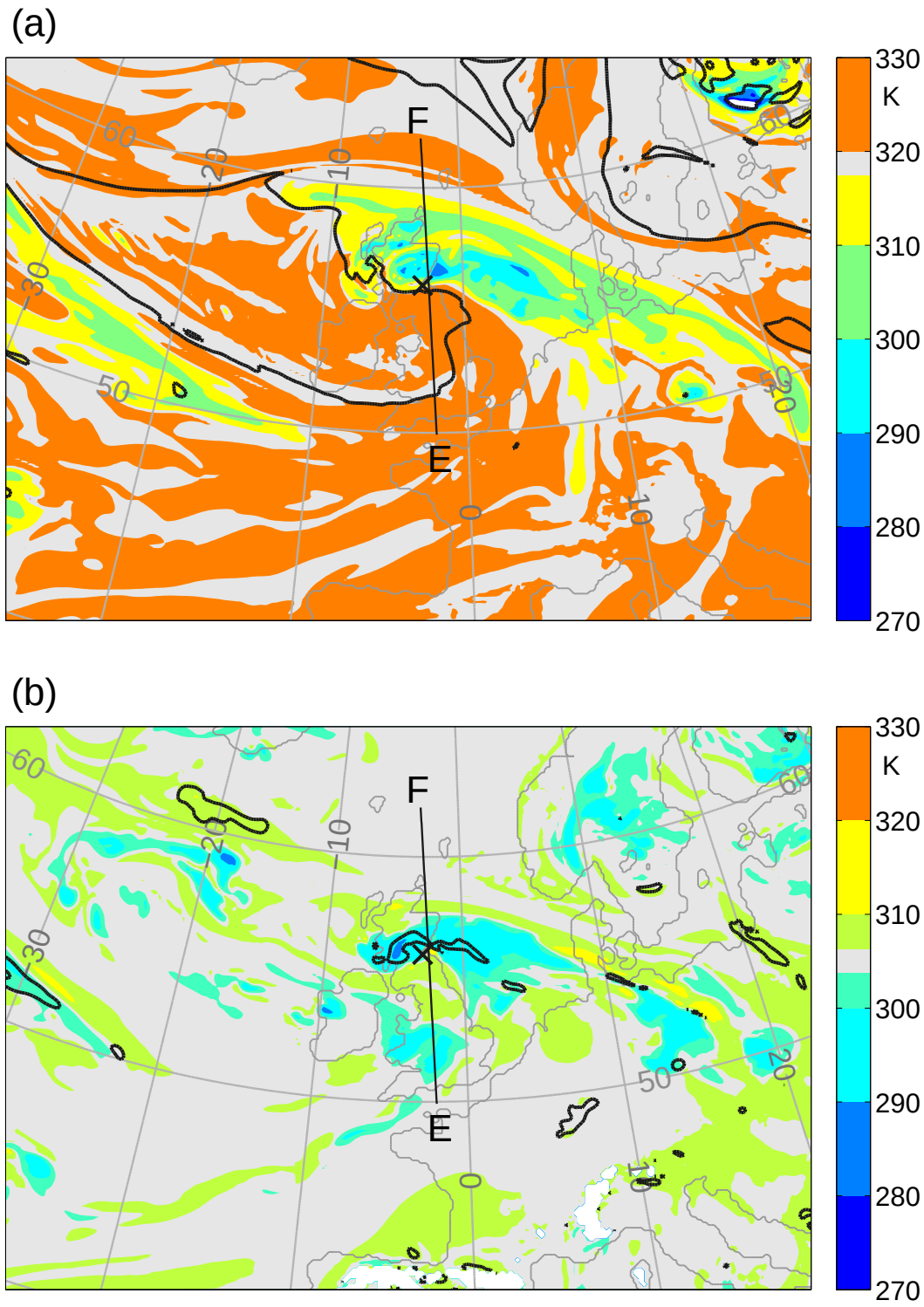

Figure 4: Maps of θ_0 tracer (color shading) at 0900 UTC 18 July 2012 (IOP13) at two isentropic levels: **(a)** 319 K and **(b)** 305 K. Bold black lines indicate 2-PVU PV contours at each isentropic level. The bold X represents the position of the low-pressure center and the segment E–F indicates the position of the sections in Figs. 5 and 6. White regions represent regions where the isentropic surfaces are not defined.

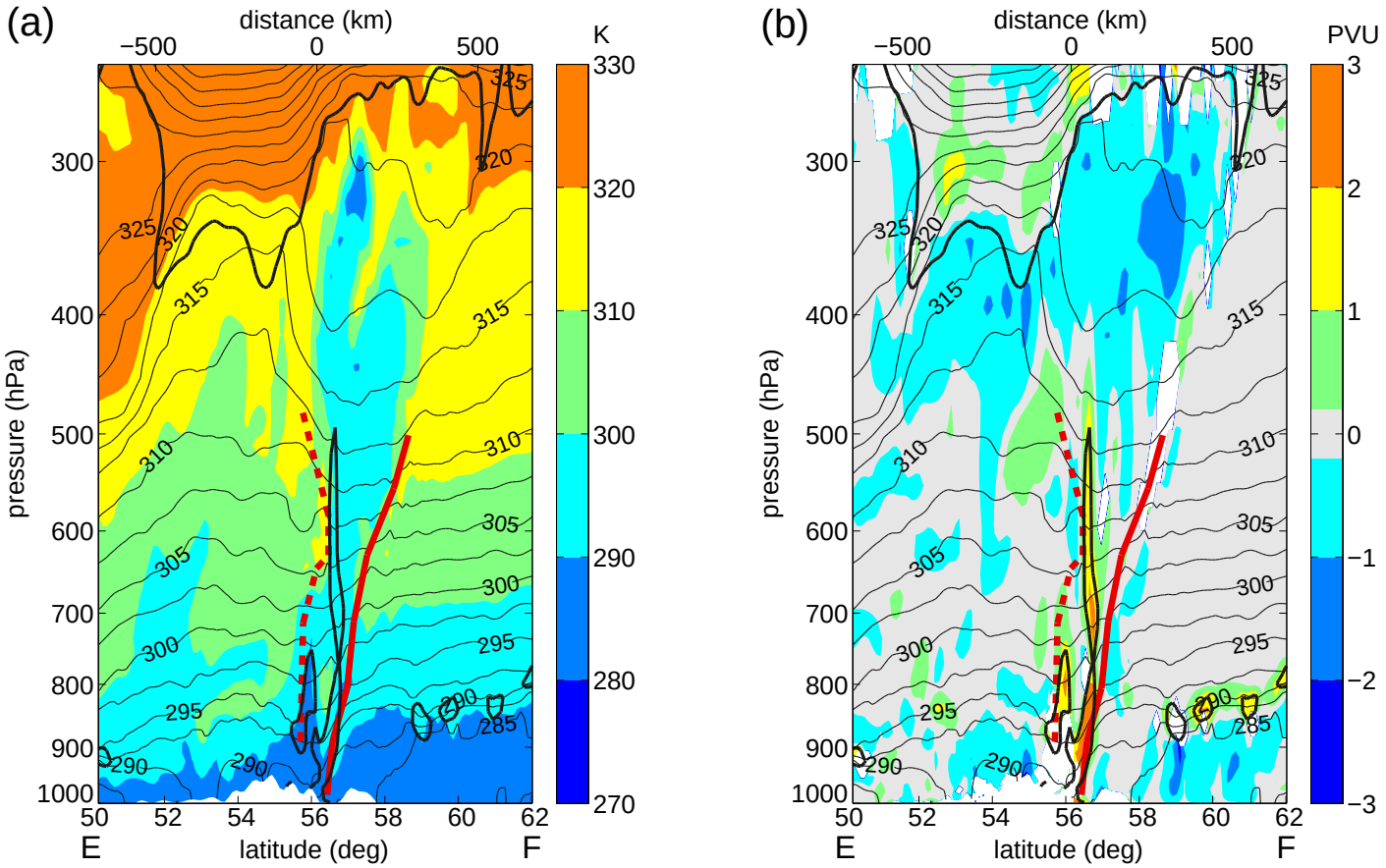

Figure 5: Vertical section along segment E–F in Fig. 4 showing in color shading (a) θ_0 and (b) total PV modification after 21 hours of integration at 0900 UTC 18 July 2012 (IOP13). In (b), grid points where PV residual error is larger than 1 PVU have been masked out (white shading). Thin black lines indicate potential temperature contours, in K, with a separation of 5 K. Bold black lines indicate 2-PVU PV contours. Bold red lines indicate the position of the system's warm (solid) and cold (dashed) fronts. The distance in the upper horizontal axis is the distance to the cyclone's center.

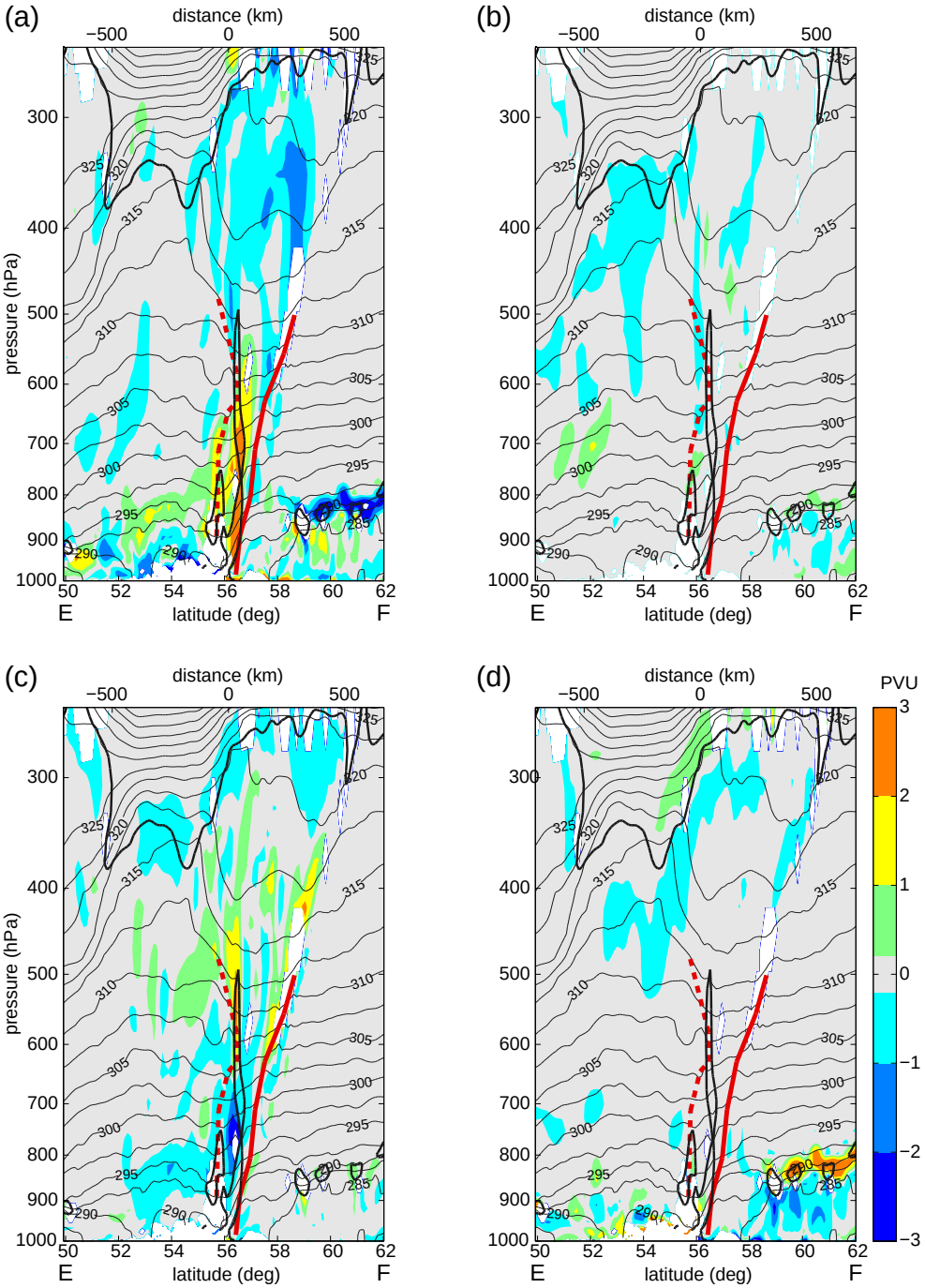

Figure 6: Vertical section along segment E–F in Fig. 4 showing in color shading contributions to PV modification from (a) BL and turbulent mixing, (b) convection, (c) cloud microphysics and (d) radiation after 21 hours of integration at 0900 UTC 18 July 2012 (IOP13). Grid points where PV residual error is larger than 1 PVU have been masked out. Thin black lines indicate potential temperature contours, in K, with a separation of 5 K. Bold black lines indicate 2-PVU PV contours. Bold red lines indicate the position of the system's warm (solid) and cold (dashed) fronts.

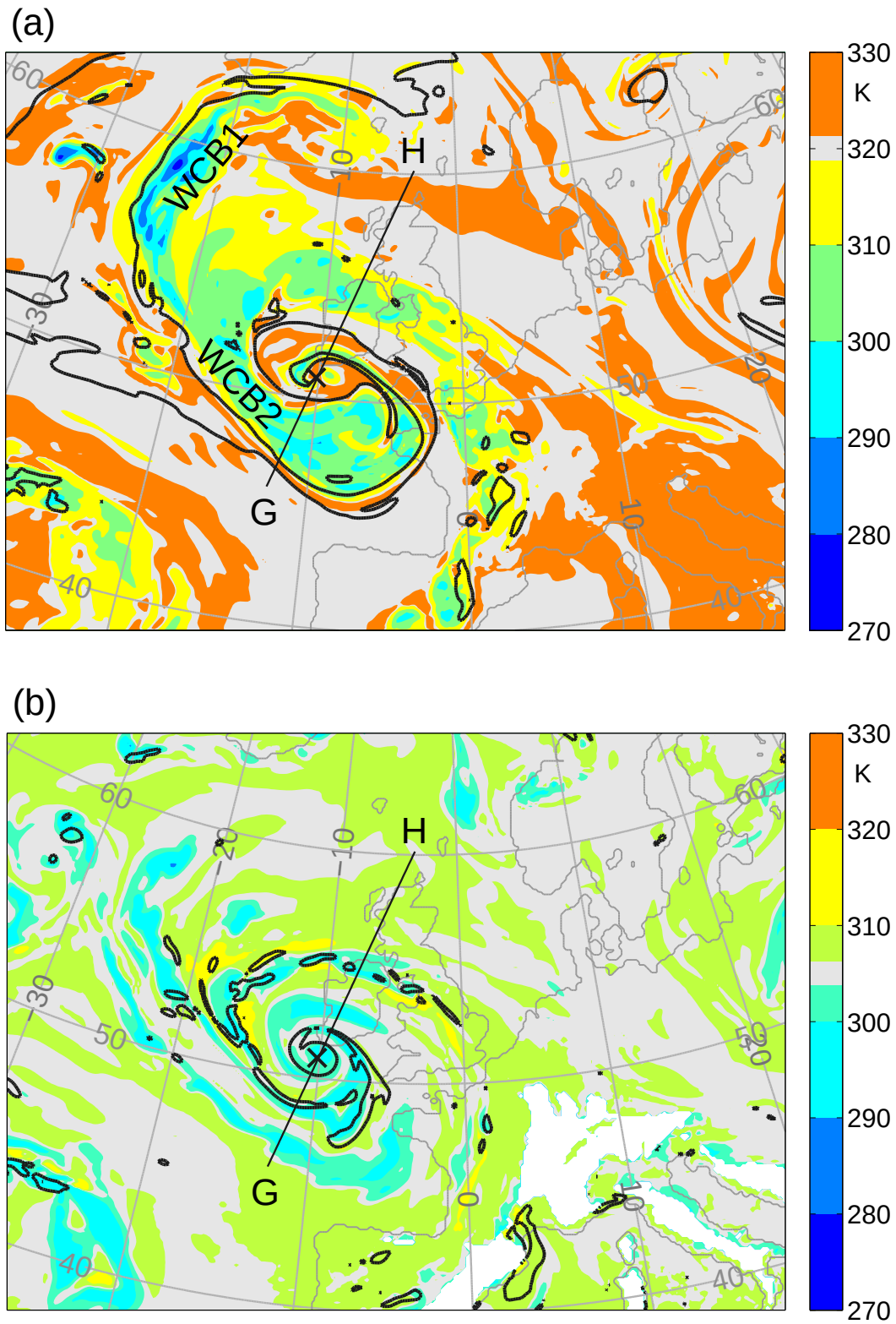

Figure 7: Maps of θ_0 tracer (color shading) at 1500 UTC 15 August 2012 (IOP14) at two isentropic levels: (a) 320 K and (b) 305 K. Bold black lines indicate 2-PVU PV contours at each isentropic level. The bold X represents the position of the low-pressure center and the segment G–H indicate the position of the vertical sections in Figs. 8 and 9. White regions represent regions where the isentropic surfaces are not defined.

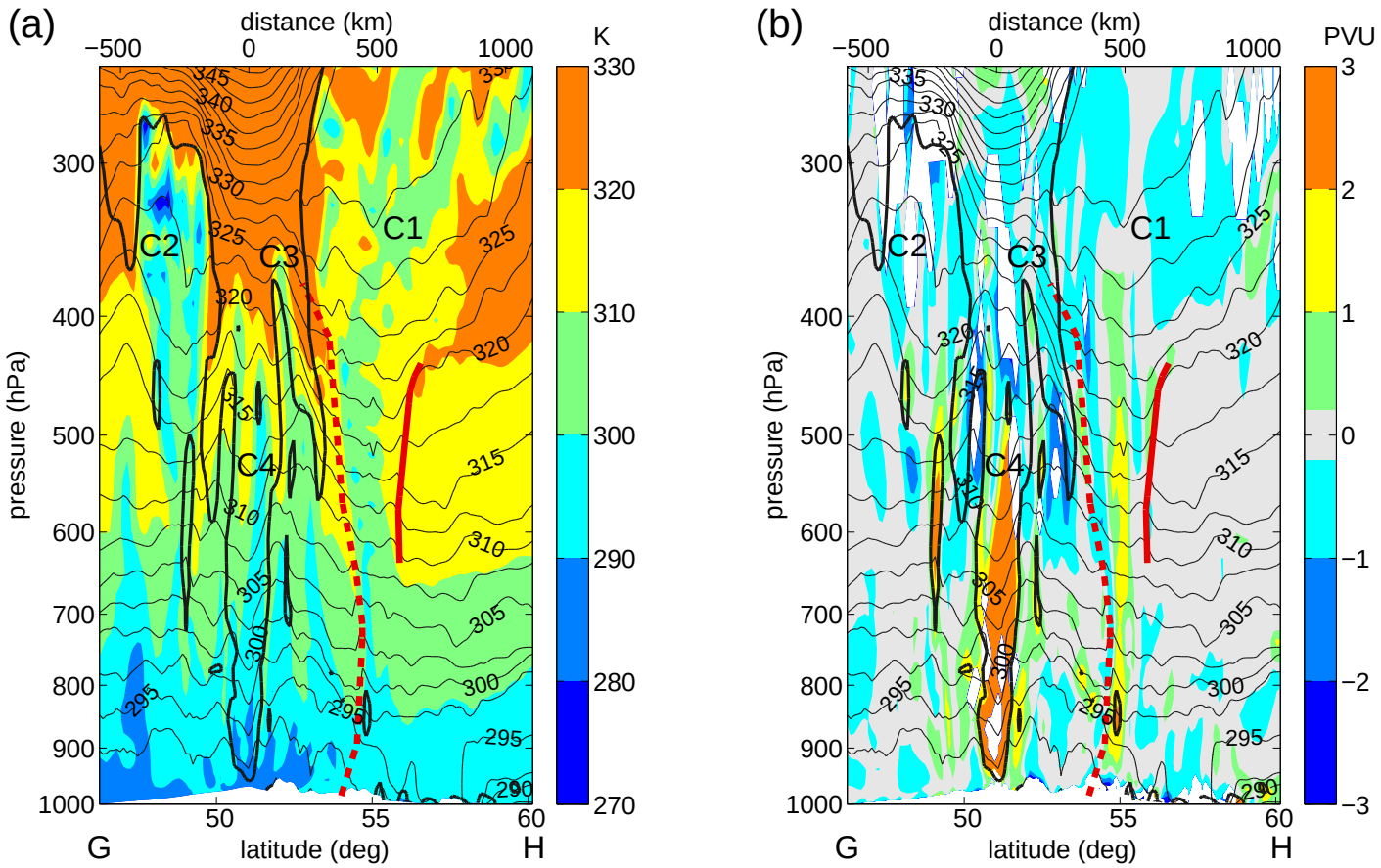

Figure 8: Vertical section along segment G–H in Fig. 7 showing in color shading (a) θ_0 and (b) total PV modification after 21 hours of integration at 1500 UTC 15 August 2012 (IOP14). In (b), grid points where PV residual error is larger than 1 PVU have been masked out. Thin black lines indicate potential temperature contours, in K, with a separation of 5 K. Bold black lines indicate 2-PVU PV contours. Bold red lines indicate the position of the system's warm (solid) and cold (dashed) fronts. Labels C1, C2 and C3 represent the position of columns of cross-isentropic ascent.

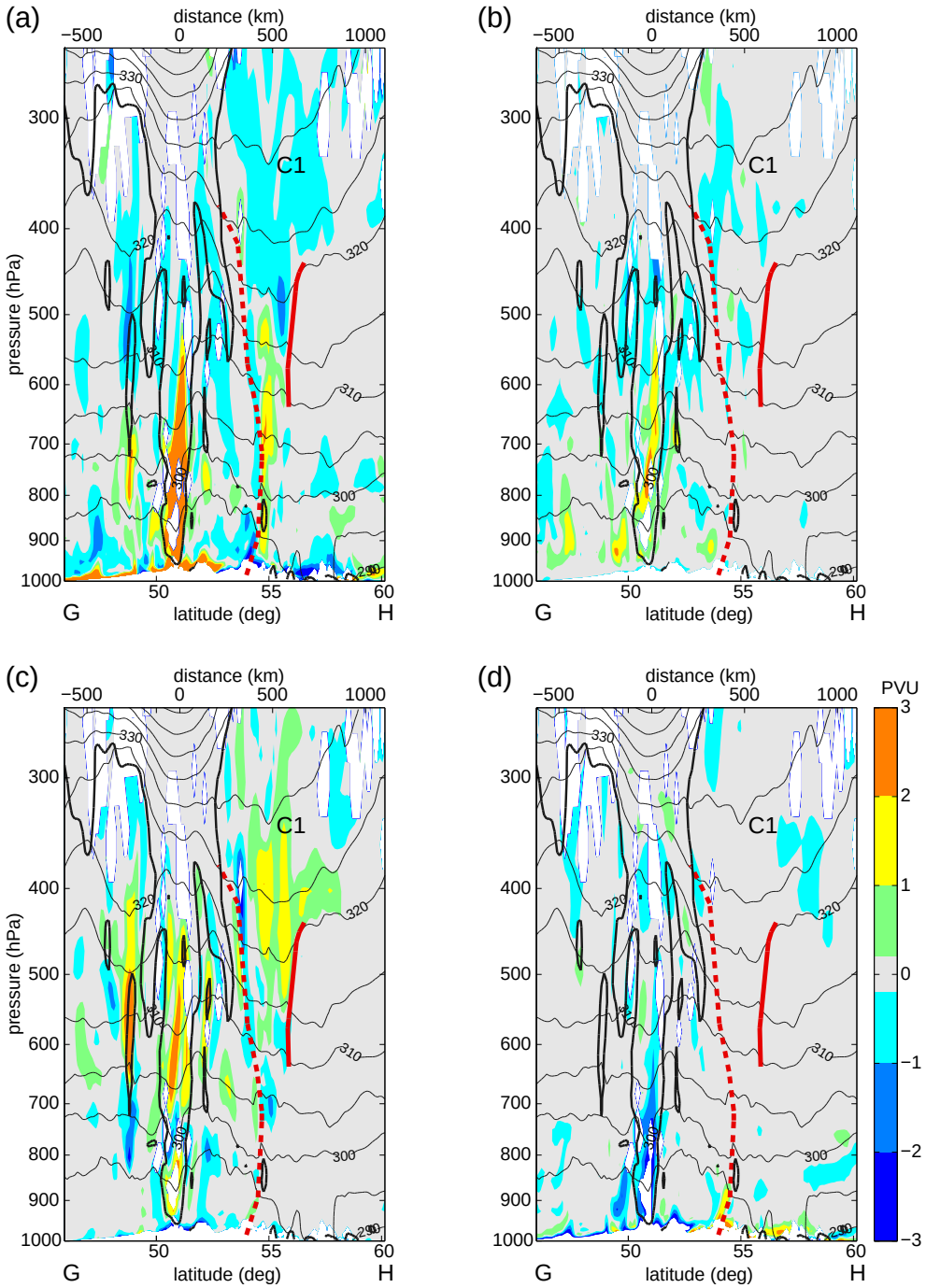

Figure 9: Vertical section along section G–H in Fig. 7 showing in color shading contributions to PV modification from (a) BL and turbulent mixing, (b) convection, (c) cloud microphysics and (d) radiation after 21 hours of integration at 1500 UTC 15 August 2012 (IOP14). Grid points where PV residual error is larger than 1 PVU have been masked out (white shading). Thin black lines indicate potential temperature contours, in K, with a separation of 5 K. Bold black lines indicate 2-PVU PV contours. Bold red lines indicate the position of the system's warm (solid) and cold (dashed) fronts. Labels C1 represent the position of of the strongest columns of cross-isentropic ascent.

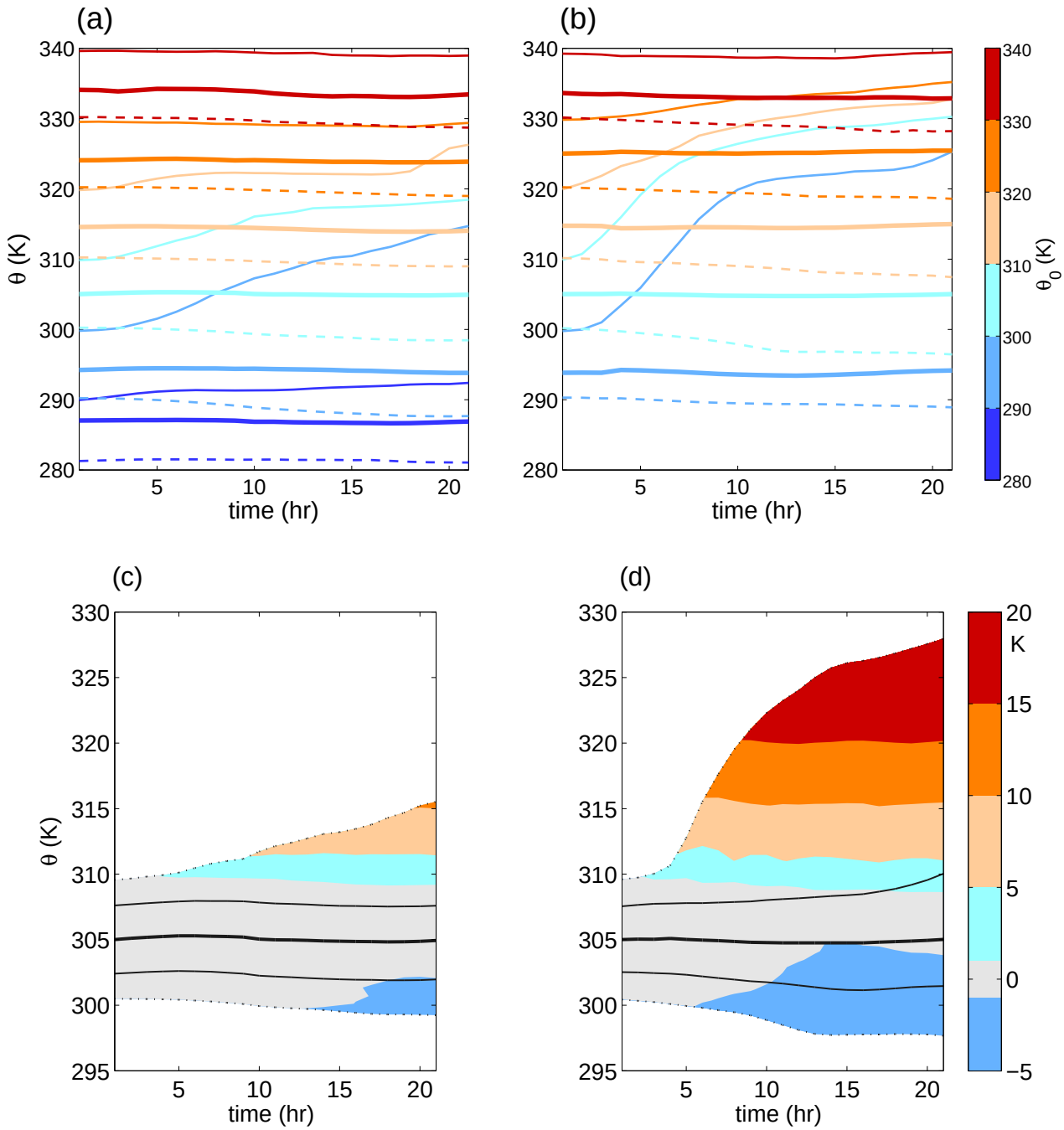

Figure 10: **(a,b)** Cross-isentropic mass transport within a 1000-km spherical cap concentric to the cyclone for **(a)** IOP13 and **(b)** IOP14. The lines are colored according to the θ_0-bin whose PDF they represent. Dashed lines, bold solid lines and thin solid lines represent the 2.5$^{\text{th}}$, 50$^{\text{th}}$ and 97.5$^{\text{th}}$ percentiles, respectively, for each θ_0-bin. **(c,d)** Heating in the bin with $300 < \theta_0 \leq 310$ [K] in a 1000-km spherical cap concentric to the cyclone for **(c)** IOP13 and **(d)** IOP14. Bold lines represent medians; thin lines represent the 25$^{\text{th}}$ and 75$^{\text{th}}$ percentiles; dotted lines represent the 5$^{\text{th}}$ and 95$^{\text{th}}$ percentiles.

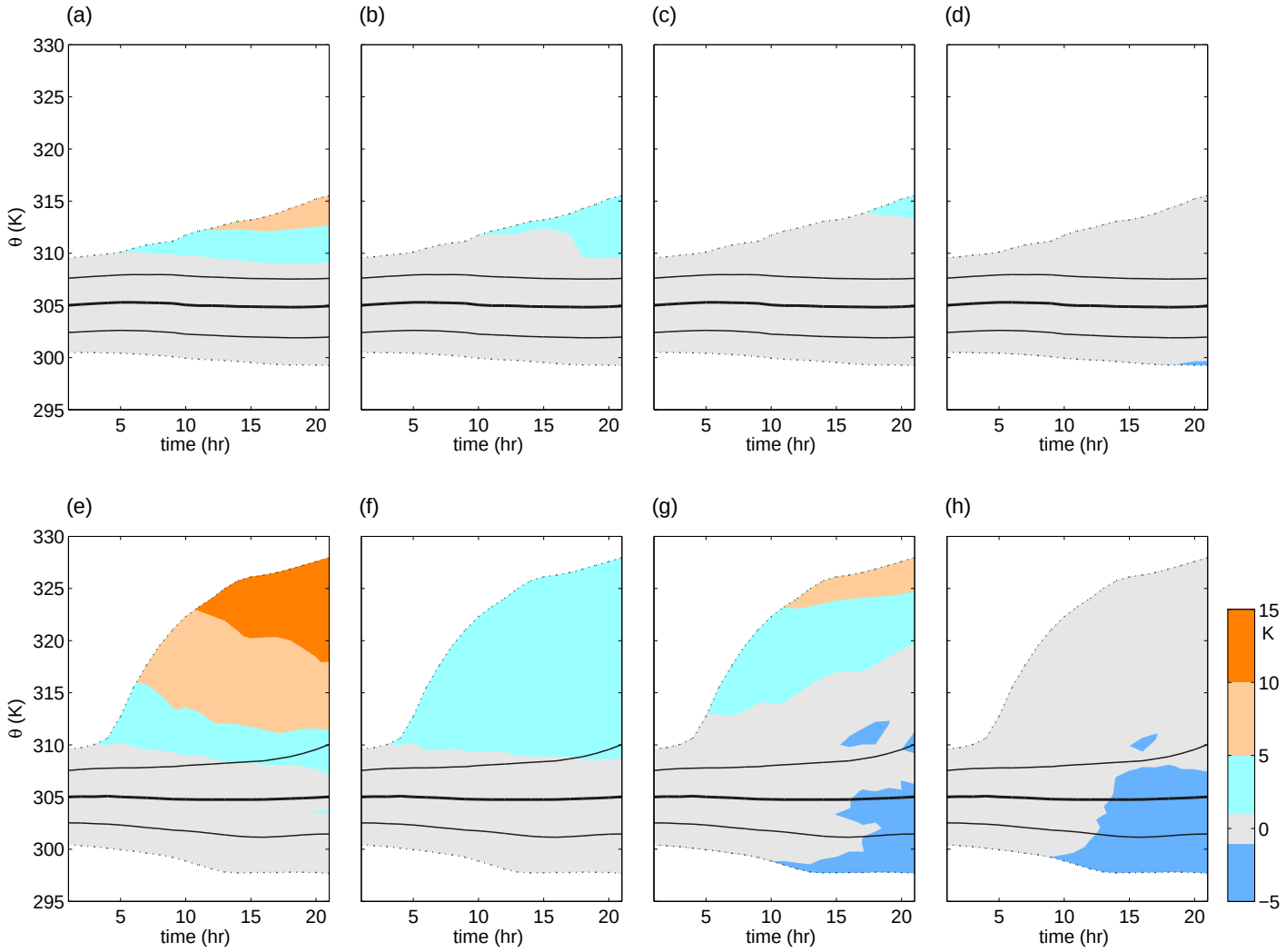

Figure 11: Heating due to the parametrization of **(a,e)** BL and turbulent mixing, **(b,f)** convection, **(c,g)** cloud microphysics and **(d,h)** radiation for the bin with $300 < \theta_0 \leq 310$ [K] in a 1000-km spherical cap concentric to the cyclone for **(a-d)** IOP13 and **(e-h)** IOP14. Bold lines represent medians; thin lines represent 25^{th} and 75^{th} percentiles; dotted lines represent 5^{th} and 95^{th} percentiles

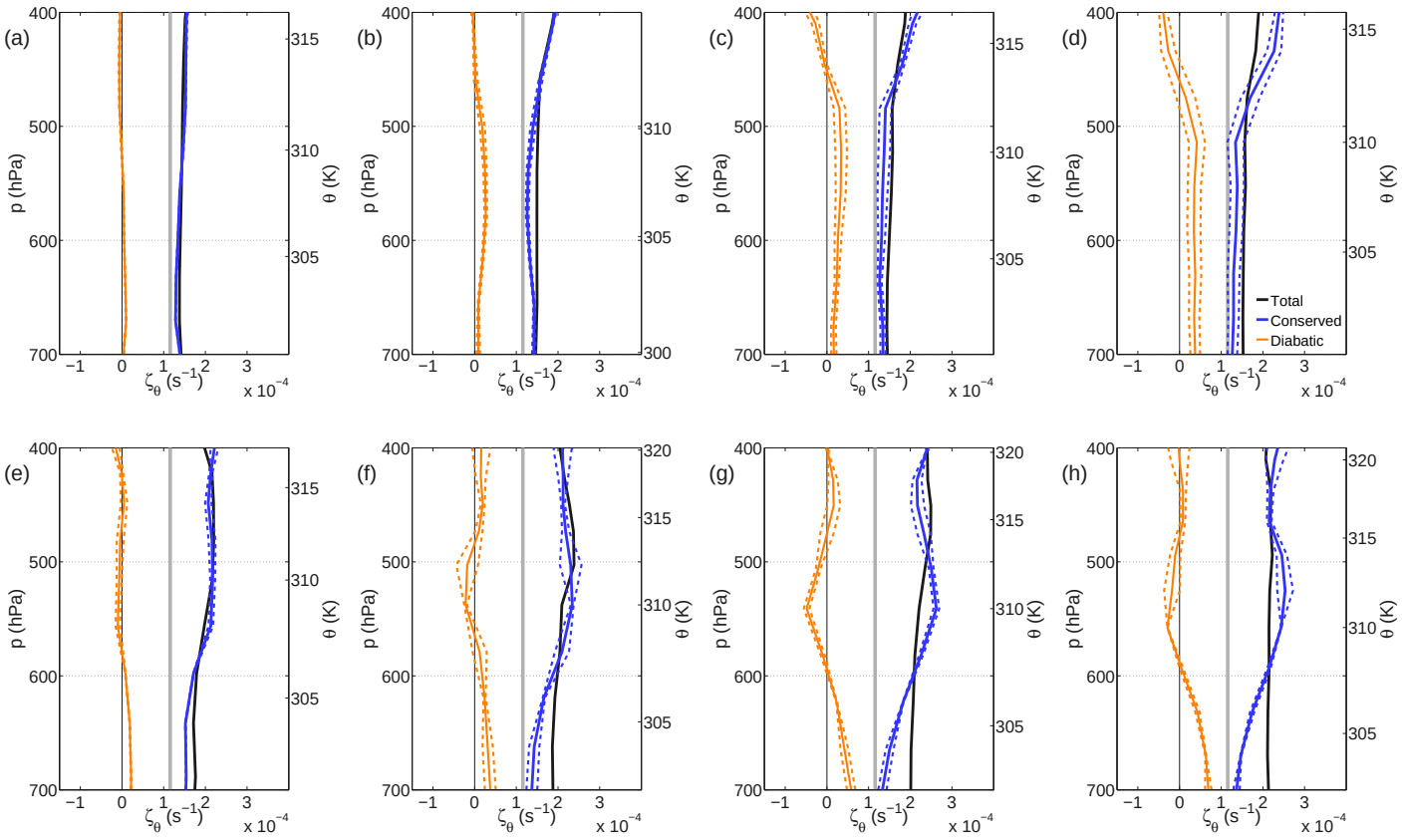

Figure 12: Vertical profiles of average isentropic vorticity (black) for a 500-km spherical cap concentric to the cyclone for **(a–d)** IOP13: **(a)** 1500 UTC, **(b)** 2100 UTC 17 July 2012, **(c)** 0300 UTC, **(d)** 0900 UTC 18 July 2012, and **(e–h)** IOP14: **(e)** 2100 UTC 14 August 2012, **(f)** 0300 UTC, **(g)** 0900 UTC, **(h)** 1500 UTC 15 August 2012. The frames also show contributions from conserved PV (blue) and diabatically-generated PV (orange), and the value of planetary vorticity at the position of the cyclone's center (gray vertical line). The dashed lines represent the conserved and diabatically-generated PV contributions with the contribution from the residual added and subtracted as an indication of uncertainty.

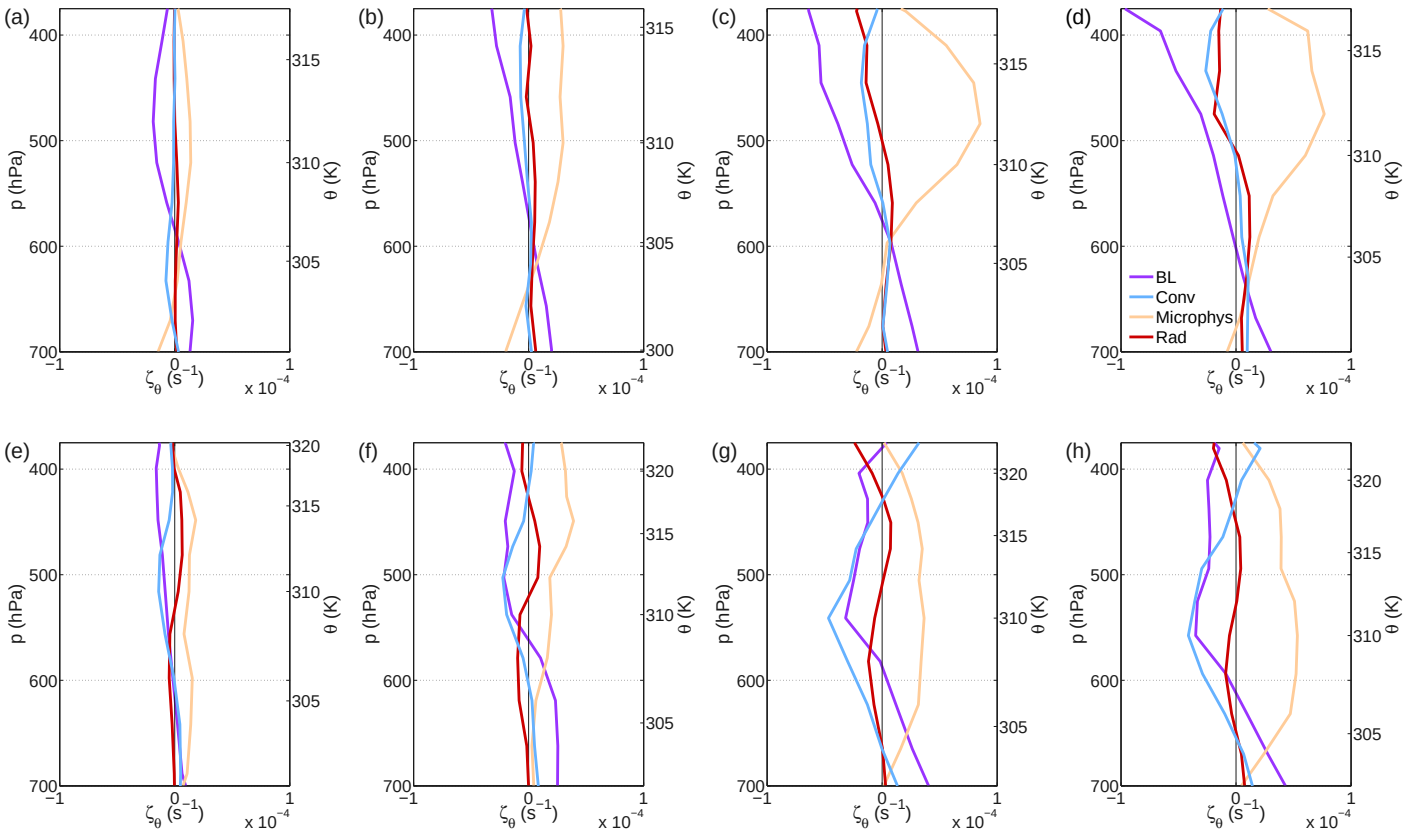

Figure 13: Vertical profiles of contributions of BL and turbulent mixing processes (BL), parametrized convection (Conv), cloud microphysics processes (Microphys) and radiation (Rad) to average isentropic vorticity for a 500-km spherical cap concentric to the cyclone for **(a–d)** IOP13: **(a)** 1500 UTC, **(b)** 2100 UTC 17 July 2012, **(c)** 0300 UTC, **(d)** 0900 UTC 18 July 2012, and **(e–h)** IOP14: **(e)** 2100 UTC 14 August 2012, **(f)** 0300 UTC, **(g)** 0900 UTC, **(h)** 1500 UTC 15 August 2012.